Atmospheric Dynamics of a Saharan Dust Outbreak over Mindelo, Cape Verde Islands: Multi-scale Observational Analyses and Simulations

saroj Dhital[1], Michael L. Kaplan[2], Jose Antonio Garcia Orza[3], and Stephanie Fiedler[4]

[1]Desert Research Institute
[2]Embry-Riddle Aeronautical University
[3]University Miguel Hernández
[4]University of Cologne

November 26, 2022

Abstract

We investigate the synoptic precursors to the Harmattan wind and dust frontogenesis during the high impact Saharan dust outbreak over the Cape Verde Islands on 13 November 2017. We employ multi-scale observations including ship data and Weather Research and Forecasting model Coupled with Chemistry simulations. The analyses indicate that the dust storm was initiated on the leeside of the Saharan Atlas Mountains (SAM) in Algeria on the 10. This dust storm was associated with a double Rossby Wave Break (RWB) linked through non-linear wave reflection. Two successive RWB contributed to the wave amplification over the Eastern North Atlantic Ocean which transported large magnitude potential vorticity air into the North African continent. The resulting coupled pressure surge was associated with cold air advected equatorward over the SAM which organized the strong near-surface wind that ablated the dust. The simulation results indicate that the dust front was initially related to a density current which formed due to the cold airflow over the SAM. The density current then triggered undular bores on the leeside. Each bore perturbed the dust loading and then the subsequent diurnal heating generated differential planetary boundary layer (PBL) turbulence kinetic energy strengthening the dust frontogenesis. Dust became confined behind the cold surge and interacted with the daytime Saharan PBL leading to increased dust loading while the dust front propagated equatorward. Two distinct dust plumes arrived successively at low-levels at Mindelo, Cape Verde Islands; (1) from the coasts of Mauritania and Senegal and (2) from the SAM southern flank.

Atmospheric Dynamics of a Saharan Dust Outbreak over Mindelo, Cape Verde Islands: Multi-scale Observational Analyses and Simulations

S. Dhital[1], M. L. Kaplan[1,2] , J. A. G. Orza[3], and S. Fiedler[4]

[1]Division of Atmospheric Sciences, Desert Research Institute, 2215 Raggio Parkway, Reno, NV 89512, USA. sdhital@nevada.unr.edu

[2]Applied Meteorology Program, Embry-Riddle Aeronautical University, 3700 Willow Creek Road, Prescott, AZ 86301, USA. kaplanm1@erau.edu

[3]SCOLAb, Department of Applied Physics, Universidad Miguel Hernández de Elche, Av. de la Universidad s/n, 03202 Elche, Spain. ja.garcia@umh.es

[4]Institute of Geophysics and Meteorology, University of Cologne, Pohligstr. 3, 50969 Köln, Germany. stephanie.fiedler@uni-koeln.de

Corresponding author: Saroj Dhital (sdhital@nevada.unr.edu)

Key Points:

- Multi-scale dynamical analysis of a Saharan dust outbreak causing strong impacts in the Cape Verde Islands in the early Harmattan season.
- A double Rossby wave break and the linking non-linear wave reflection are instrumental for dust emission and subsequent transport.
- Density current-induced undular bores and the planetary boundary layer turbulence kinetic energy strengthened the dust frontogenesis.

Abstract

We investigate the synoptic precursors to the Harmattan wind and dust frontogenesis during the high impact Saharan dust outbreak over the Cape Verde Islands on 13 November 2017. We employ multi-scale observations including ship data and Weather Research and Forecasting model Coupled with Chemistry simulations. The analyses indicate that the dust storm was initiated on the leeside of the Saharan Atlas Mountains (SAM) in Algeria on the 10th. This dust storm was associated with a double Rossby Wave Break (RWB) linked through non-linear wave reflection. Two successive RWB contributed to the wave amplification over the Eastern North Atlantic Ocean which transported large magnitude potential vorticity air into the North African continent. The resulting coupled pressure surge was associated with cold air advected equatorward over the SAM which organized the strong near-surface wind that ablated the dust. The simulation results indicate that the dust front was initially related to a density current which formed due to the cold airflow over the SAM. The density current then triggered undular bores on the leeside. Each bore perturbed the dust loading and then the subsequent diurnal heating generated differential planetary boundary layer (PBL) turbulence kinetic energy strengthening the dust frontogenesis. Dust became confined behind the cold surge and interacted with the daytime Saharan PBL leading to increased dust loading while the dust front propagated equatorward. Two distinct dust plumes arrived successively at low-levels at Mindelo, Cape Verde Islands; (1) from the coasts of Mauritania and Senegal and (2) from the SAM southern flank.

1 Introduction

The mineral dust mobilized in drylands of North Africa, the largest and most prominent active dust source on Earth (e.g., Prospero et al., 2002; Washington et al., 2003) can be transported for several thousands of kilometers, e.g., equatorward (e.g., Prospero & Mayol-Bracero, 2013; Van der Does et al., 2018) and/or poleward (e.g., Moulin et al., 1998; Pey et al., 2013; Solomos et al., 2018; Varga et al., 2013). During boreal winter (November to April), the northeasterly/easterly low-level trade winds in North Africa, also known as Harmattan wind, transport a large fraction of mobilized dust towards the tropical Atlantic Ocean (Prospero, 1999; Prospero & Mayol-Bracero, 2013) and impacts the human environment downwind through the degradation of air quality and visibility, affecting air-traffic, and infrastructures. Nearly half of the dust suspended over the Sahel region is associated with the Harmattan wind (Klose et al., 2010). However, the large-scale dust storms associated with the Harmattan wind are challenging to forecast because of the aperiodic nature of surges in trade winds even though the most substantial dust emission over the northern fringes of North Africa is associated with Harmattan surges (Fiedler et al., 2015).

The Harmattan wind commonly develops as a result of the intensification of the meridional pressure difference over the Sahara Desert (Burton et al., 2013) and is associated with a positively tilted upper-level trough (Fiedler et al., 2015). The sudden intensification of the anticyclone in association with a strong pressure surge over North Africa, strong low-level jet stream maximum, and a cold air outbreak from the Mediterranean cause a strong Harmattan surge (Kalu, 1979). The post-frontal strengthening of the strong isallobaric-ageostrophic low-level wind caused by pronounced upper-level convergence, sinking, and anti-cyclogenesis over north-western Africa often also cause Harmattan surges (Knippertz & Fink, 2006).

Ubiquitous multi-faceted research has been carried out to understand the dynamics of dust emission and subsequent long-range transport of dust associated with the Harmattan surge because of its significant contribution to atmospheric dust loading (Fiedler et al., 2015; Knippertz & Fink, 2006; Pokharel et al., 2017). Pokharel et al. (2017) discovered that low-level isallobaric-ageostrophic winds are associated with meso-β scale adjustment processes that led to the widely studied March 2004 extreme Harmattan surge. Additionally, their study also highlighted that both Kelvin waves and Mountain-Plains Solenoid (MPS) circulations, formed as a result of meso-β and meso-γ scale adjustment processes near and over the Atlas Mountains, were responsible for causing a major dust storm over North Africa. The study by Fiedler et al. (2015) on the climatology of Harmattan surges discovered that the rapid increase in pressure in the cold air over northwest Africa results in the above-threshold isallobaric-ageostrophic wind near the surface that is critical for dust ablation. Also, many field campaign experiments were performed in or near the Cape Verde Islands to characterize and quantify the dust transported from North Africa (Gama et al., 2015). However, the evolution of meso-β scale processes such as density currents, undular bores, and subsequent dust frontogeneses during the Harmattan season have not been studied in detail before. To this end, we perform here in-depth analyses with new high-resolution numerical simulations for the dust outbreak in mid-November 2017. For this dust outbreak, ship-based aerosol optical measurements were made during a research expedition offshore of West Africa (Fiedler, 2018), where observations are otherwise rare.

The Cape Verde Islands, which lie 650 km off the coast of Senegal, West Africa are mostly affected by the Saharan dust outbreak during winter, as the Harmattan wind carries a higher concentration of dust at low-levels during this season (Gama et al., 2015). Recently, a strong continental-scale Saharan dust outbreak was observed in satellite imagery over Mindelo, Cape Verde on 13 November 2017, reducing horizontal visibility to ~1100 m and leading to significant disruptions of local air traffic. Dust mobilization was already observed on the foothills of the Saharan Atlas Mountains (100 in Figure1a and Figure1b) at 0600 UTC 10 November 2017 but did not appear clearly in MSG-SEVIRI dust images on subsequent days. This indicates the difficulty of understanding complex linkages in Harmattan events thus justifying the need to understand the meteorological dynamics associated with such a strong continental-scale dust storm to improve dust storm forecasting. Improvements that could result in the reduction of Harmattan dust storms' immediate adverse impact upon air quality, public health, aviation, road safety, and other infrastructure. This study presents the first multi-scale dynamical analysis of the meteorological processes involved in this dust outbreak over the Cape Verde Islands and aims to answer the following questions: (1) which synoptic scenario allowed a favorable condition for the windy, cold surge that resulted in dust deflation on the lee side of the Saharan Atlas Mountains, (2) what was the spatio-temporal evolution of the accompanying meso-β scale density current, undular bore, and dust frontogenesis, (3) what are the roles of Saharan complex terrain and well-mixed Saharan atmospheric boundary layer (SABL) in the westward advection of dust aerosols, and (4) what is the implication of high-resolution simulations with Weather Research and Forecasting model Coupled with Chemistry (WRF-CHEM) for operational dust forecasting of this type of phenomenon? We perform a high-resolution WRF-CHEM simulation with horizontal resolutions of up to 2km and use available observational data, including the unique dust observations obtained from the 2017 North Atlantic Expedition to help answer the preceding questions. To our knowledge, this is the first time that the spatio-temporal evolution of dust frontogenesis is described with such a high-resolution version of the WRF-CHEM model. This work is motivated by the North Atlantic expedition MSM68/2 of the research vessel Maria S. Merian (Fiedler, 2018) from Germany to Cape Verde between 3 and 14 November 2017.

This paper is organized as follows. In section 2, we describe the data and methodology employed in this research. In section 3, we present the synoptic precursor to the Harmattan wind indicating the occurrence of a double RWB. Section 4 presents the evolution of dust frontogenesis and the comparison between simulation results and the observations. The summary and conclusions of the multi-scale processes responsible for this dust outbreak appear in section 5.

2 Methodology

2.1 Observations

The analysis of the spatio-temporal evolution of dust makes use of seven different observations datasets: (1) false-color dust imagery from the Spinning Enhanced Visual and Infrared Imager (SEVIRI) onboard the geostationary Meteosat Second Generation (MSG) satellites, (2) the observational dataset of pressure, wind, visibility, and temperature from Meteorological Terminal Aviation Routine Weather Report (METAR), (3) surface synoptic observations (SYNOP), (4) the sounding dataset at different stations provided by the University of Wyoming (http://weather.uwyo.edu/upperair/sounding.html), (5) the aerosol subtype data from the Cloud-Aerosol Lidar and Infrared Pathfinder Satellite Observations (CALIPSO), (6) the aerosol optical depth (AOD) dataset from the Moderate Resolution Imaging Spectroradiometer (MODIS) (https://ladsweb.modaps.eosdis.nasa.gov/), and (7) the AOD measurements from the North Atlantic expedition (Fiedler, 2018). The satellite imagery and AOD data provided the time and location of the occurrence of dust aerosols and allowed us to follow the dust plumes for cloud-free regions. Observations from METAR and SYNOP were used to find the time and location of reduced visibility due to the dust storm. The available METAR and SYNOP observation stations over the study area are shown in Figure 1a. The radiosonde dataset provided information on the vertical structure of the thermal and wind fields during and before the formation of the dust storm.

The synoptic-scale meteorological analyses were performed using the European Center for Medium-Range Weather Forecast (ECMWF) ERA-Interim reanalysis dataset (Dee et al., 2011). We used the charts of potential vorticity (PV), Montgomery stream function (TSI) and horizontal wind on the 330 K isentropic surface to understand the upper-level dynamics and the role of RWB. RWB occurs during nonlinear wave amplification. Charts of mean sea-level pressure (MSLP), 925 hPa winds, and potential temperature were employed to analyze the near-surface conditions. We further diagnose trajectories of air parcels arriving in Mindelo, Cape Verde to understand the transport paths of the dust aerosols. To this end, we use the NOAA Hybrid Single-Particle Lagrangian Integrated Trajectory (HYSPLIT) model (Stein et al., 2015) initialized with the ERA-Interim dataset.

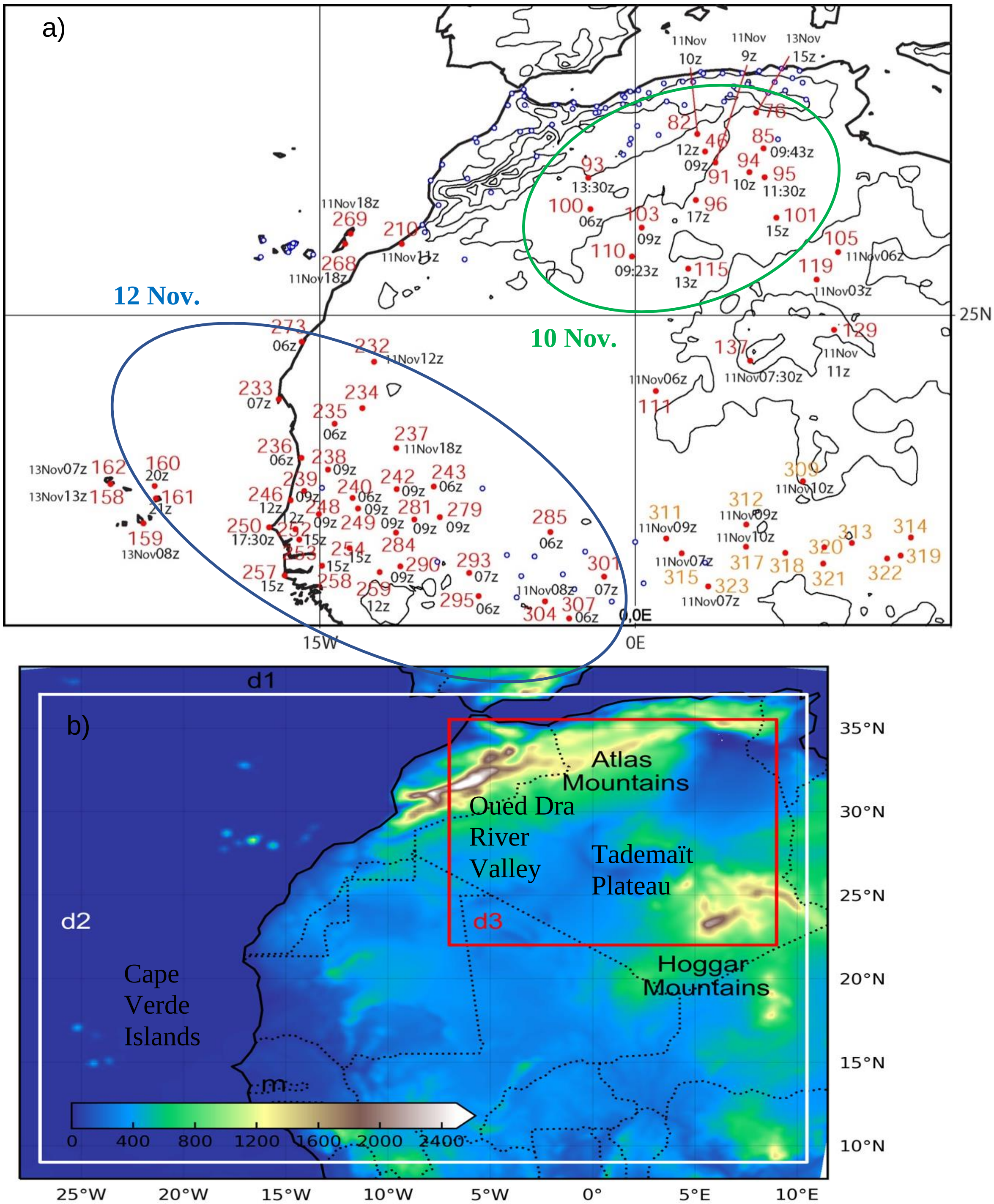

Figure 1. The location of METAR and SYNOP stations over Northwest Africa and the Cape Verde Islands are shown by circles (a), where the red ones indicate the stations that recorded horizontal visibility lower or equal to 5km on the 10th (green oval) and 12th (blue oval). The date and hour in the plot represent the time of reduction in visibility. Topography of Northwest Africa and the surrounding region with WRF-CHEM simulation domains (d1-3) (b).

2.2 High-resolution simulations

To describe the meso-β/γ scale meteorological features that are critical for dust emission and subsequent transport, we performed high resolution numerical simulations with 18 and subsequently additional nested domains with 6km and 2km horizontal grid spacings utilizing the WRF-CHEM model version 3.9 (Grell et al., 2005). The 18km simulation domain includes most of North Africa, some parts of the Mediterranean Sea, and the Eastern Atlantic Ocean (Figure 1b). The model atmosphere was divided into 40 vertical levels. Simulations were initialized with ERA-Interim reanalysis data at 0000 UTC (18km), 0600 UTC (6km), and 1200 UTC (2km) November 9, and ending at 1800 UTC November 13 (18km and 6km) and 1800 UTC November 11 (2km), respectively.

The moist convective parameterization scheme was employed on the coarsest resolution only using the Betts-Miller-Janjic scheme (Janjic, 1994). We switched off the moist convection parameterization in the high-resolution inner domains (6km and 2km) and therefore explicitly resolved moist convection on the model grid. This approach is needed to better represent the convection and associated cold pools or density currents (Reinfried et al., 2009; Heinold et al., 2013; Roberts & Knippertz, 2014). Our model configurations are otherwise identical across the different resolutions with: (1) the double-moment bulk microphysical parameterization (Thompson et al., 2008), (2) the Mellor-Yamada-Janjic (MYJ) planetary boundary layer scheme (Janjic, 2002; Mellor & Yamada, 1974), (3) the Noah Land Surface Model (Chen & Dudhia, 2001; Ek et al., 2003) developed jointly by the National Center for Atmospheric Research (NCAR) and National Centers for Environmental Prediction (NCEP), (4) the Dudhia shortwave scheme (Dudhia, 1989), and (5) Rapid Radiative Transfer Model (RRTM) for longwave radiation scheme (Mlawer et al., 1997).

We employed the WRF-CHEM model in a dust-only mode utilizing the Georgia Tech/Goddard Chemistry Aerosol Radiation and Transport (GOCART) dust scheme (Ginoux et al., 2001). The WRF-CHEM model includes five dust bins having effective radii of 0.73, 1.4, 2.4, 4.5, and 8 μm. The model outputs the dust Aerosol Optical Depth (AOD) at 550 nm using the corresponding columnar mass load and the extinction efficiencies at 550 nm for each of the sub-bins. The GOCART dust scheme simulates the uplifted dust flux as a function of wind speed, erodibility, and the wetness of the surface. The emission flux (F_p) is calculated as:

$$F_p = CSs_p u^2_{10m}\left(u_{10m} - u_t\right) \qquad \text{if } u_{10m} > u_t \qquad (1)$$

with the constant $C = 1\ \mu g m^{-5} s^2$. The source function S is a dimensionless quantity, which depends upon soil properties. s_p is the mass fraction of size group p of dust emission, u_{10m} is the wind at 10-meter height and u_t is the threshold wind velocity for the effects of wind erosion. The detailed explanation of the GOCART dust scheme can be obtained from Ginoux et al. (2001).

3 Observational analysis

3.1 Evolution of the dust outbreak

The initial signal of the dust storm was recorded by the SYNOP station at Beni-Abbes (100 in Figure 1a) on the southern flank of the Saharan Atlas Mountains in Algeria at 0600 UTC on the 10th. This station reported a visibility of 2000 m, NNW wind of 10.3 m/s, and a MSLP of

1015 hPa at that time. However, the freshly emitted dust did not appear in the SEVIRI image due to the presence of regional clouds (Figure 2a). Six hours later, at 1200 UTC, the Beni-Abbes station recorded a visibility of 4000 m and a higher MSLP of 1018.3 hPa. At the same moment, a dust plume was visible in the SEVIRI image on the southern foothills of the Saharan Atlas Mountains (note thick red circle in Figure 2b). Within that 6-hour period, the MSLP in the Beni-Abbes region increased by 3.3 hPa and visibility remained less than 4000 m. These meteorological features and the signal of dust in the SEVIRI image suggest that the strong near-surface wind associated with the pressure surge lifted the available dust from the foothills of the Saharan Atlas Mountains higher into the atmosphere.

At a later stage, a dust front formed that led this dust as it propagated further equatorward under the influence of the pressure surge. By a "dust front" we are using the dust analog to a temperature front or a first-order discontinuity of observed dust. It passed the In-Salah weather station in Algeria by 1310 UTC (115 in Figure 1a) which reported a horizontal visibility of 1400 m and wind speed of 11.3 m/s. The pressure continued to rise at Beni-Abbes, where the station recorded a MSLP of 1021.3 hPa by 1800 UTC. Within 12 hours of this time, the pressure increased by 6.3 hPa over a significant region on the lee side of the Saharan Atlas Mountains. This MSLP increase is rapid compared to the maximum MSLP increase during the March 2004 extreme Harmattan surge. During this March 2004 period, MSLP increased by 6.9 hPa within 24-hours near the Algeria-Mali border (Knippertz & Fink, 2006).

At 0000 UTC on the 11th, the dust front broadened and covered the entire southwestern region of Algeria (see the black line in Figure 2c). The dust front then continued moving equatorward, where it covered nearly the entire region of south-west Algeria, north-east Mauritania, and northern Mali (note black line in Figure 2d) by 1200 UTC on the 11th. At the same time, the Zouerate SYNOP station in Mauritania (232 in Figure 1a) reported the dust storm with a visibility of 3000 m, an easterly wind of 10 m/s, and a MSLP of 1016.7 hPa.

The dust storm reached the West African coast by 0000 UTC on the 12th but was not visible in the SEVIRI image even in the absence of clouds (Figure 2e). At 0600 UTC, the nearby Nouakchott SYNOP station (236 in Figure 1a) in Mauritania recorded an easterly wind of 6 m/s and visibility of 2000 m. The visibility was sharply reduced to 800 m by 1200 UTC. Also, the visibility was already starting to decrease in the eastern part of the Cape Verde Islands by 0300 UTC on the 12th. At this time, the METAR station named Boa Vista Rabil (161 in Figure 1a) in Cape Verde reported a northeasterly wind with a horizontal visibility of 5000 m. The visibility remained less than 5000 m for 4 hours. The sky remained clear from 0800 UTC to 2000 UTC. But after 2000 UTC on the 12th, the visibility again was less than 5000 m until 2300 UTC on the 13th with a significant reduction to 1600 m from 0900 UTC to 1400 UTC. The succeeding reduction in visibility at the Boa Vista Rabil station in the Cape Verde Islands indicates the occurrence of two dust plumes, which led to the closure of the local airport on Sao Vicente.

This observational analysis of the dust evolution suggests that the dust storm was initiated on the southern flank of the Saharan Atlas Mountains as a result of strong near-surface wind under the influence of a strong pressure surge, as in the case of a classical Harmattan surge (e.g., Fiedler et al. 2015, Pokharel et al., 2017). Two distinct dust plumes reached the Cape Verde Islands in succession, nearly 45 hours after the initial phase of the storm, where the large-scale plume followed a smaller dust plume (the differences between these plumes will be discussed in Section 4.2.1).

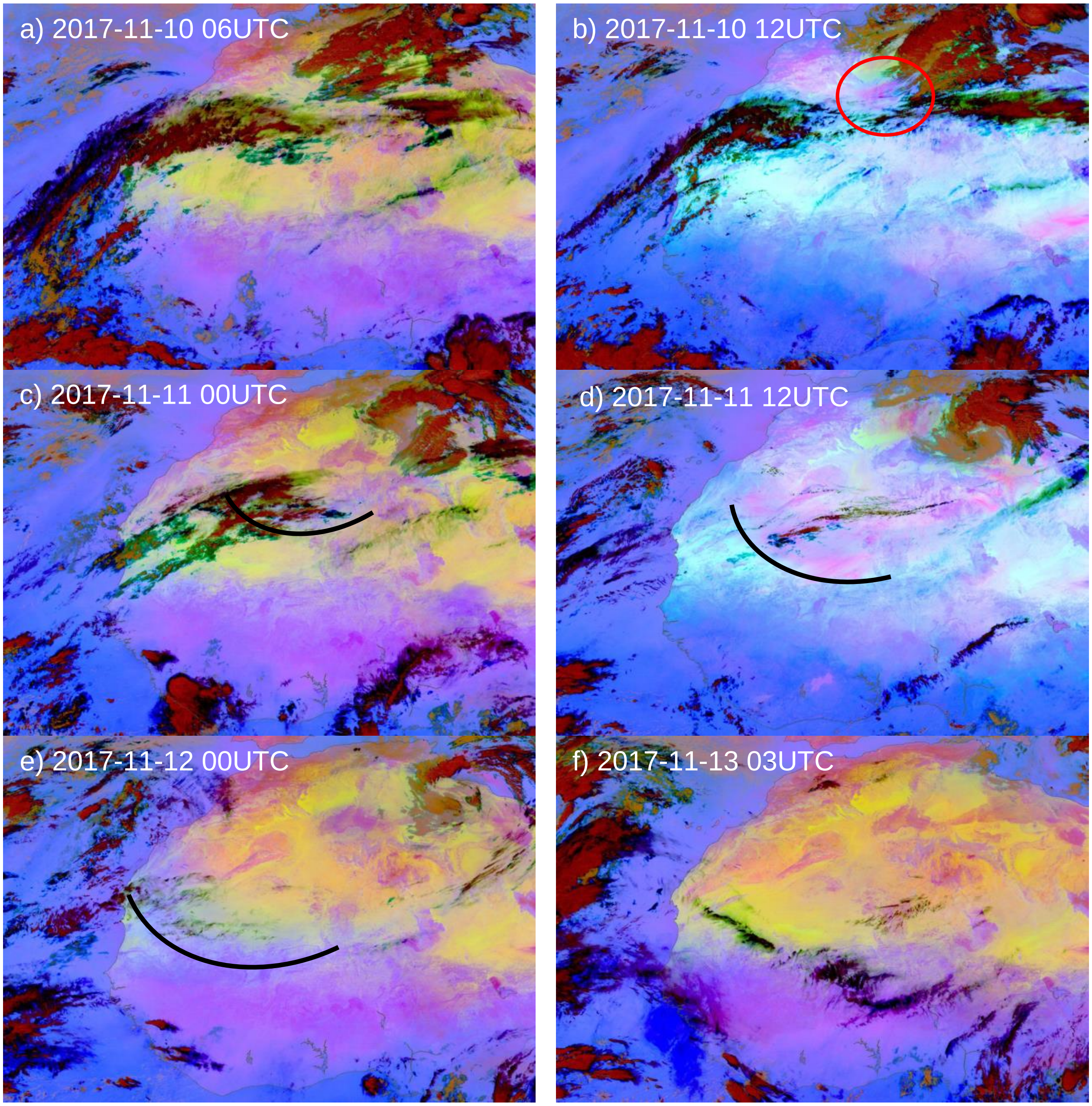

Figure 2. Sequence of MSG-SEVIRI dust RGB images that illustrate the evolution of the dust storm: (a) 0600 UTC 10 November, (b) 1200 UTC 10 November, (c) 0000 UTC 11 November, (d) 1200 UTC 11 November, (e) 0000 UTC 12 November, and (f) 0300 UTC 13 November. The red circle and the solid black lines indicate the region of dust emission on the lee side of the Saharan Atlas Mountains and the leading edge of the propagating dust storm, respectively.

3.1.2 Vertical structure of wind and temperature

The inter-comparison of the 24-hour vertical structure of the wind and temperature on the 10th and 11th, before and during the passage of the front, based on the Bechar radiosonde station for 0000 UTC and the In-Salah station for 1200 UTC, is presented in Figure 3. At the Bechar station (93 in Figure 1a), where the dust front was observed after 0000 UTC on the 10th, the sounding at 0000 UTC on the 11th showed the development of the low-level north-northeasterly flow with substantial cooling up to 700 hPa with maximum cooling (~13ºC) at the 850 hPa level between 10 and 11 November (Figures 3a and 3b). Farther equatorward, the front has passed the In-Salah weather station (115 in Figure 1a, equatorward of the Tademaït Plateau) by 1310 UTC on the 10th. The In-Salah sounding at 1200 UTC on the 11th indicated significant cooling up to 650 hPa with strong northerly flow (Figures 3c and 3d) and, specifically, nearly 10ºC cooling near the ground. The substantial reduction in lower-tropospheric temperature and the radical change in wind direction to the north indicate that strong cold advection from the northern latitudes must have occurred during this episode.

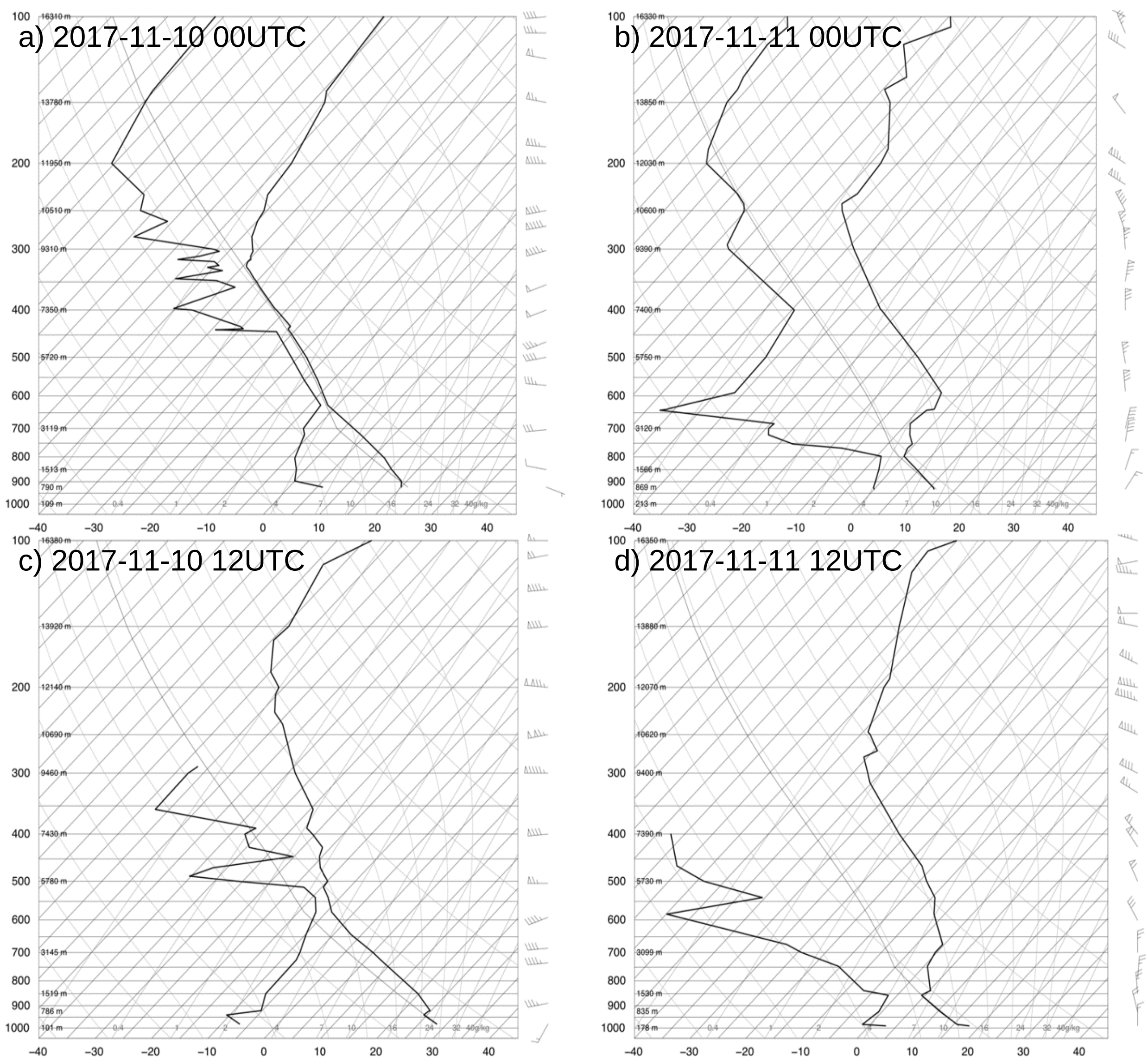

Figure 3. Skew T-log p diagrams for Bechar station (31.61ºE, 2.23ºN) at 0000 UTC on the 10th (a) and 11th (b), and In-Salah station (2.5ºE, 29.2ºN) at 1200 UTC on the 10th (c) and 11th (d) in Algeria.

3.2 Synoptic-scale precursors

Two RWB occurred setting the environment for the later dust storm development. The first RWB started ~5-6 days before the formation of the dust storm and a second RWB occurred just before the onset of the evolution of the dust storm. RWB#1 occurred during 5-7 November over the northeastern Atlantic Ocean, offshore of northwestern Africa, as indicated by the reversal of the PV gradient near 30°N over the Eastern Atlantic Ocean (see the black rectangular box in Figures 4a, 4b, and 4c). Also, cold air propagated into the northwestern part of North Africa as indicated by the low value of TSI resulting from the trough thinning consistent with RWB (e.g., Postal and Hitchman, 1990). This equatorward intrusion of high PV air resulted in upper-level winds adjusting to the mass field, leading to the strengthening of the Subtropical jet (STJ). Following RWB#1, a strong PV ridge formed over the northeast Atlantic Ocean and became quasi-stationary (Figures 4d and 4e). RWB#2 followed during 8-10 November as a result of non-linear wave amplification and trough thinning over the southern Iberian Peninsula (IP) and the northwestern fringe of North Africa (see the green rectangular box in Figures 4d, 4e, and 4f). This process led to the formation of a massive PV ridge over the North Atlantic Ocean and trough over the western part of the Mediterranean as indicated by the TSI fields in Figures 4d, 4e, and 4f.

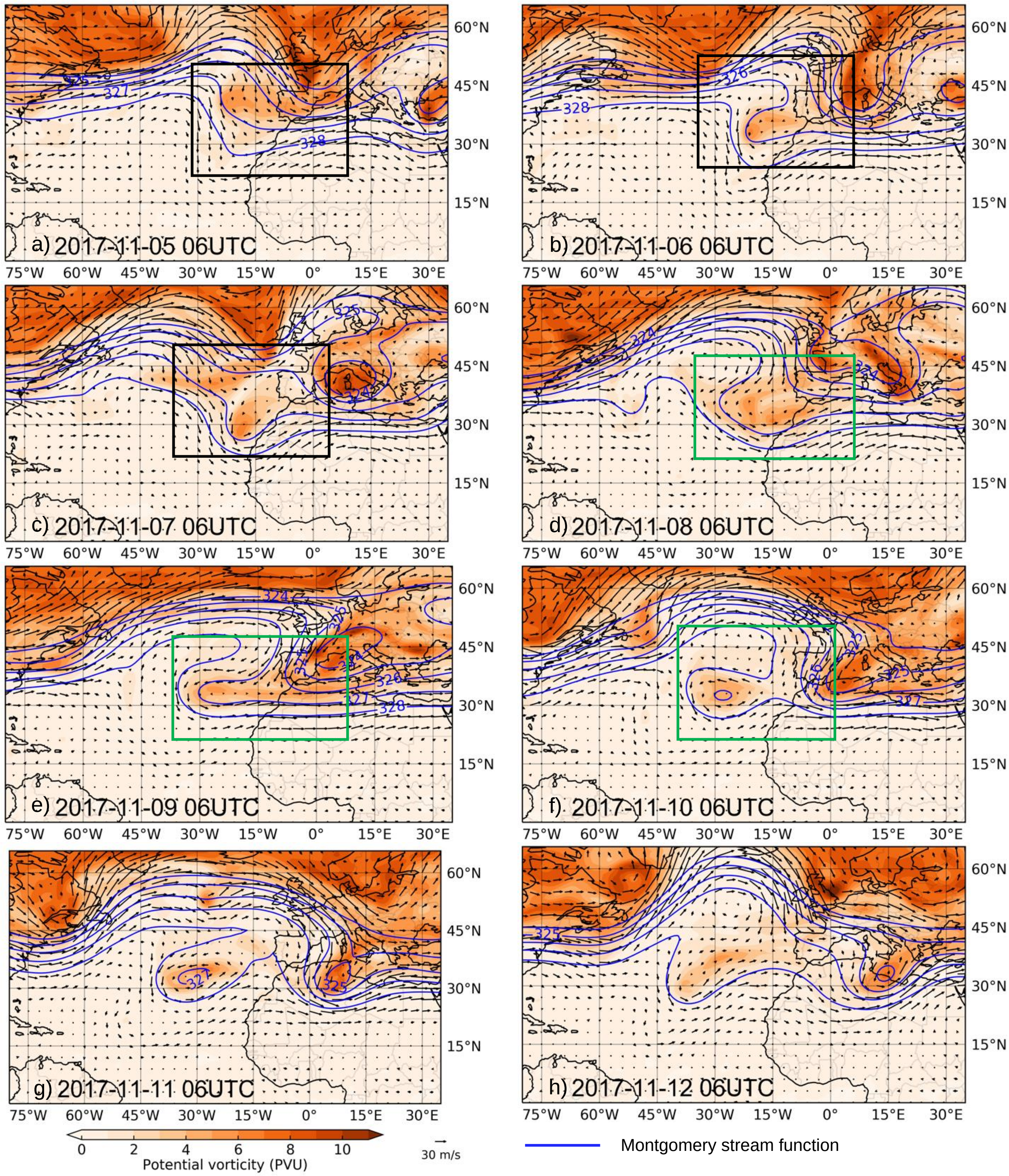

Figure 4. ERA-Interim horizontal cross-sections of potential vorticity (shaded), wind vectors, and Montgomery stream function (blue counters) at the 330K IPV surface indicating the dual RWBs and valid for 0600 UTC: (a) 5, (b) 6, (c) 7, (d) 8, (e) 9, (f) 10, (g) 11, and (h) 12 November 2017. The square boxes represent the region of RWB.

At the lower levels before RWB#1, two high-pressure centers were juxtaposed over the subtropical Eastern and Western Atlantic Ocean, respectively. Additionally, a large surface low was in place over the North Atlantic as well as a weak low pressure over the eastern Mediterranean Basin (Figure 5a). During RWB#1, at 0600 UTC 6 November, the eastern subtropical high pressure started to drift northeastward consistent with the advection of an upper-level PV ridge, while the surface low started to move poleward (Figure 5b). Following RWB#1, the low-level fields were restructured, where the two subtropical high-pressure systems started to become juxtaposed and moved eastward simultaneously (Figure 5b). The cold air started to propagate into the North African continent, as indicated by the reduction of 925 hPa potential temperature in time. With the completion of the first RWB, at 0600 UTC 7 November, a single subtropical anticyclone merged and became located over the central North Atlantic (Figure 5c). The subtropical high pressure became strong and occupied a large area during RWB#2 consistent with the strong ridging in the upper-level PV field (Figures 5d, 5e, and 5f). At 0600 UTC 9 November, the subtropical anticyclone continued moving eastward very slowly and extended over the IP and the northern fringe of North Africa (Figure 5e). Following RWB#2, the intensification of the subtropical anticyclone resulted in the advection of cold air from higher latitudes into North Africa over the Saharan Atlas Mountains. The rapid pressure increase accompanying the intrusion of cold air over northwestern Africa (Figures 5g and 5h) resulted in the strong near-surface wind that is critical for dust mobilization on the lee side of the Atlas Mountains not unlike the case study of classical Harmattan surges published by Fiedler et al. (2015).

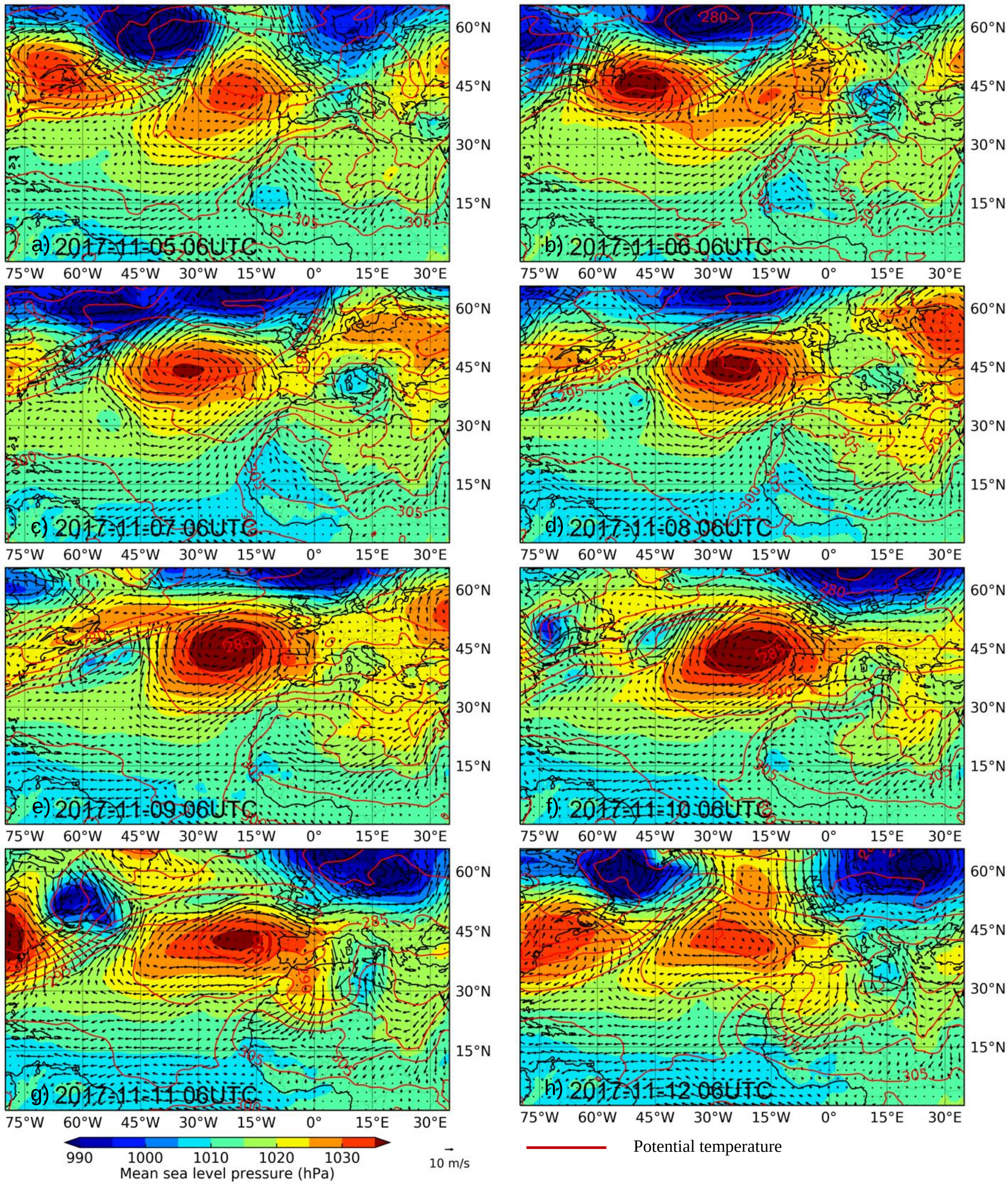

Figure 5. ERA-Interim horizontal cross-sections of mean sea level pressure (shaded), 925 hPa wind vectors, and potential temperature (red contours) valid for 0600 UTC: (a) 5, (b) 6, (c) 7, (d) 8, (e) 9, (f) 10, (g) 11, and (h) 12 November 2017.

This analysis suggests that the synoptic precursors to the near-surface wind and dust transport followed a series of RWB and non-linear Rossby wave reflection, as noted by Abatzoglou &

Magnusdottir (2004). Messori and Caballero (2015) mentioned the importance of double RWB in extreme weather, where they stressed that the most destructive storms affecting continental Europe during 1951-2001 were associated with a double RWB. The series of RWB, in this case, significantly contributed to the wave amplification over the Eastern North Atlantic Ocean and resulted in the intrusion of the very significant PV air into the North African continent aloft. The pressure surge associated with the cold air from poleward latitudes into North Africa through the Saharan Atlas Mountains resulted in the strong near-surface wind that is critical for dust deflation, as in the case of a classical Harmattan surge (Fiedler et al., 2015). Equatorward RWB over the North Atlantic Ocean has been identified in other studies to cause Saharan dust outbreaks (Wiegand & Knippertz, 2014).

4 High-resolution simulation results and trajectory analysis

4.1 Model comparisons with observations

To compare the simulated evolution of the dust in this episode, we used the aerosol subtype data from the CALIPSO, AOD from the MODIS instrument, and the Maritime Aerosol Network (MAN) of the Aerosol Robotic Network (AERONET) collected during expedition MSM68/2 (Fiedler, 2018). The vertical profile of dust was compared with the CALIPSO observations for the 10th and 13th (Figure 6). The CALIPSO images at 1322 UTC on the 10th and 0300 UTC on the 13th (Figures 6b and 6d) both, respectively, show a dust layer up to 3-km height AGL on the lee side of the Atlas Mountains during the initial phase of the dust storm and up to 2.5 km when the dust storm reached the Cape Verde Islands. Consistent with the CALIPSO observation, our simulated dust layers during these periods were mostly confined below 2-km AGL (Figures 6a and 6c).

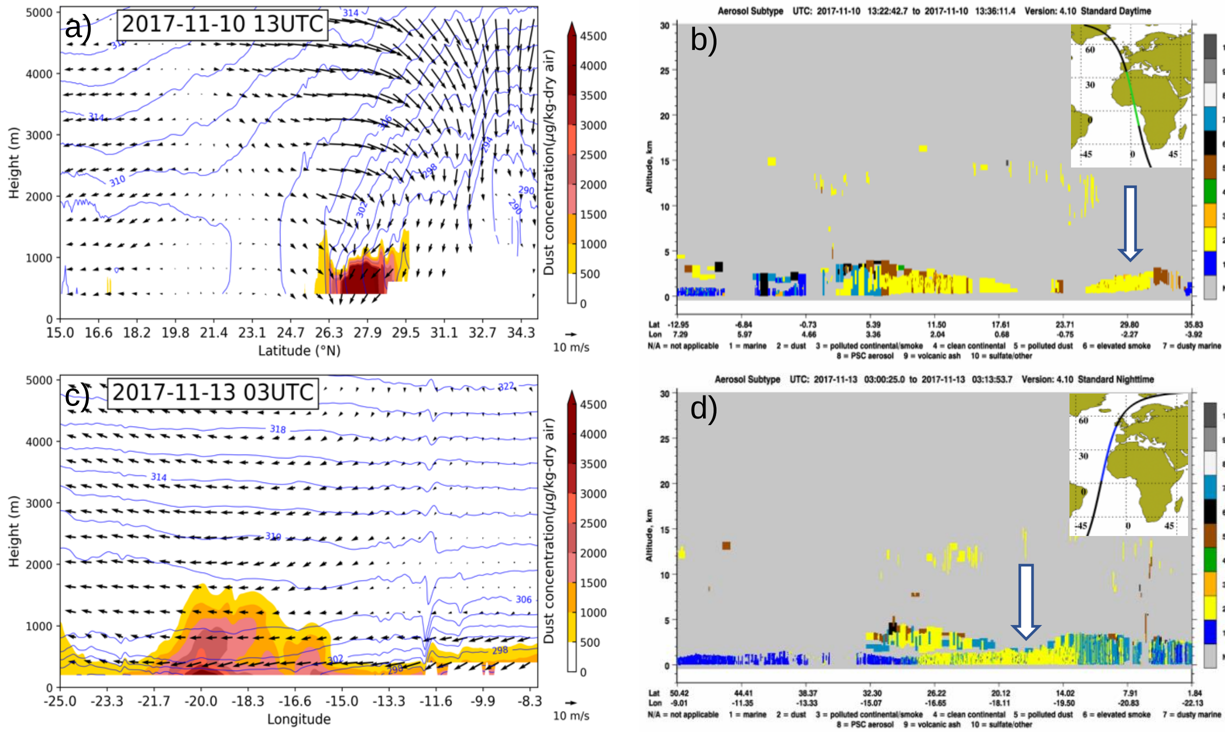

Figure 6. WRF-CHEM simulated (6-km) vertical cross-section of wind, potential temperature, and dust concentration along 2.5ºW at (a) 1300 UTC 10 November and along 16ºN at (c) 0300 UTC 13 November, and aerosol subtype from the CALIPSO observation for 10 November (b) and 11 November (d) 2017. The downward pointing white arrows denote the region of the dust layer.

The temporal evolution of the simulated dust plume was compared with the MODIS observations. The MODIS-Terra overpass at 1245 UTC on the 12th captured the AOD up to a value of 0.5 over the Cape Verde Islands, while the WRF-CHEM simulated AOD over the same region ranged from 0.1 to 0.5 (Figures 7a and 7b). At 1145 UTC on the 13th, the MODIS AOD extending from the coast of Mauritania to the offshore was almost 0.5, while the simulated AOD over the same region ranged from 0.1-0.4 (Figures 7c and 7d). These values suggest a model tendency towards AOD underestimation, but we expect some underestimation of our modeled AOD in southern regions. This is because we simulate dust aerosols only, i.e., we do not account for anthropogenic aerosol emissions, e.g., from southern West Africa, nor sea spray aerosols from the ocean, which are also seen by MODIS. Our AOD in the simulation, however, reproduces the spatio-temporal evolution of the AOD from MODIS.

Additionally, the comparison of the simulated AOD against the MSM68/2 measurements shows that the simulated AOD evolution is in reasonable agreement and reproduces the temporal evolution of the observations (Figure 8). Upon the arrival of the dust storm over Mindelo, Cape Verde at 1030 UTC on the 12th, the simulated AOD was 0.18 compared to an observation of 0.22. At 1330 UTC, the simulated AOD was 0.22, while the observed value was 0.19. These AOD values are close to one another and indicate that there is only a small difference between observations and simulations.

To summarize, the comparison between simulated and observed AOD shows that the WRF-CHEM model simulated the spatio-temporal evolution of dust over the Cape Verde Islands in this specific Harmattan dust storm with consistent and sufficient accuracy to add credibility to the simulations. This gives us confidence in using the simulations to investigate the physical processes leading to this dust outbreak, to be discussed next.

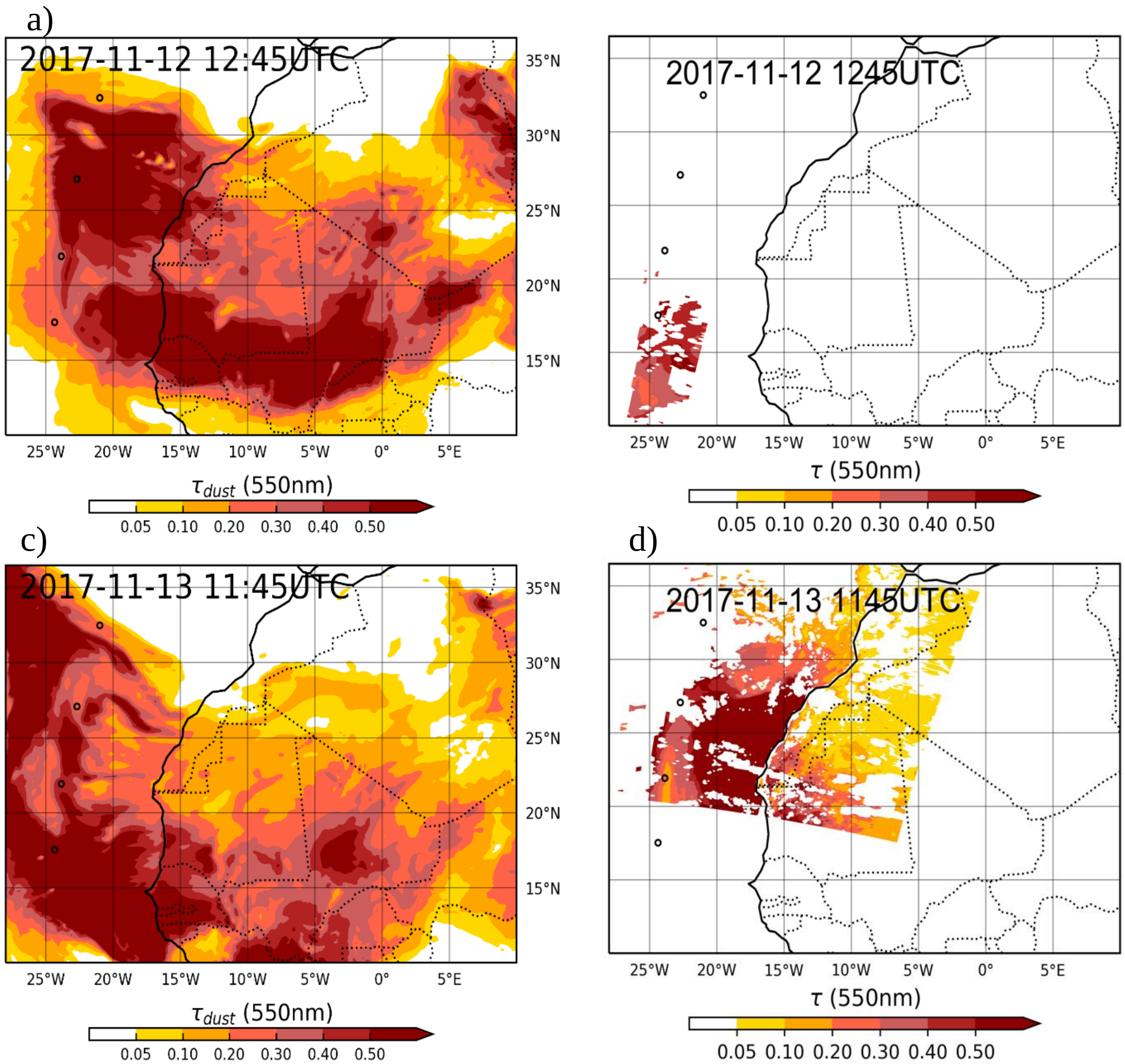

Figure 7: WRF-CHEM simulated (18-km) AOD valid for (a) 1245 UTC 12 November and (b) 1145 UTC 13 November and AOD from the MODIS for (b) 1245 UTC 12 November and (d) 1145 UTC 13 November 2017. The hollow dot represents the location of the ship during the MSM68/2 2017 North Atlantic expedition (Fiedler, 2018).

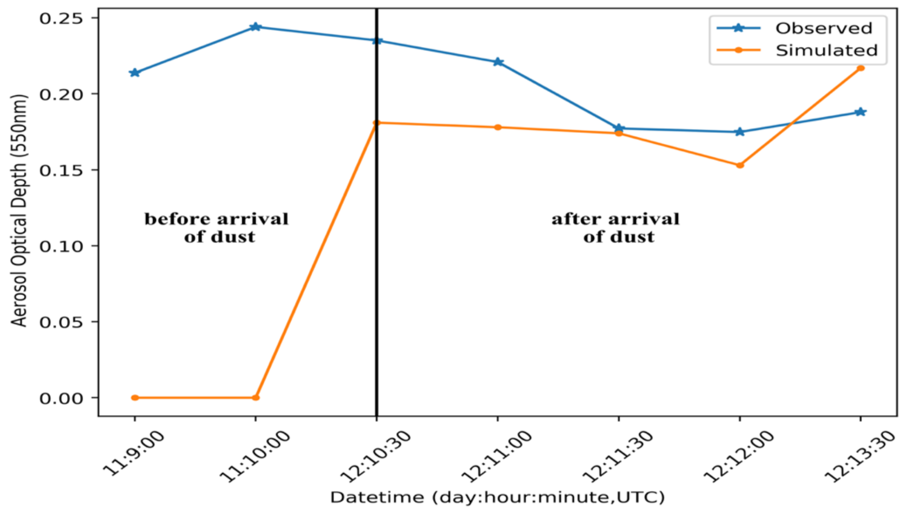

Figure 8. Comparison between WRF-CHEM simulated and observed AOD from expedition MSM68/2 on 12 November (Fiedler, 2018).

4.2 Process assessment with WRF-CHEM results

In this section, we analyze the meso-β and γ scale meteorological and dust transport processes from the WRF-CHEM simulation to show that the dust outbreak over the Cape Verde Islands was comprised of two dust plumes consistent with surface observations in the Cape Verde Islands as explained previously in Section 3.1.1. The smaller of the two dust plumes, reaching the Cape Verde Islands first, formed near the coast of Mauritania and Senegal ahead of the cold front at 1700 UTC on the 11th while the large and intense dust plume formed behind the leading edge of the cold front that initially developed on the lee side of the Saharan Atlas Mountains at 0600 UTC on the 10th. The detailed evolution of the multiple dust plumes will be discussed in section 4.2.1. Additionally, we will present the mechanisms of dust emission and the spatio-temporal evolution of dust frontogenesis in subsequent sections.

4.2.1 Evolution of simulated dust and formation of multiple dust plumes

The initial signal of dust emission on the lee side of the Saharan Atlas Mountains appeared around 1600 UTC on the 9th, near 2.5ºW, 29ºN, before the arrival of the cold front (Figure 9a), as a result of the southwesterly low-level flow near the Algeria/Morocco border. During this period, the low-pressure system was building to the south of the Atlas Mountains. Because of this intensifying low-pressure system, the southwesterly low-level flow strengthened near the Oued Dra River Valley on the Algeria/Morocco border and deflated dust, which was subsequently transferred northeastward. At 0000 UTC on the 10th, cold air propagated down the Atlas Mountains and the strong near-surface wind associated with this cold surge emitted a significant amount of dust representing the incipient stage of the dust storm (Figure 9d). The size of the dust plume then expanded as it propagated downstream (Figures 9e and 9f). The spatial evolution of the simulated dust at 1200 UTC on the 10th is qualitatively consistent with the SEVIRI image (Figures 2a and 9f).

As the dust front propagated downstream, the spatial extent of the dust plume increased substantially. However, the dust loading started to decrease by 0000 UTC on the 11th. It became a minimum at 0700 UTC (Figure 10a) as the PBL stabilized inhibiting the mixing process. By 0800 UTC, dust loading again started to increase and became a maximum around 1700 UTC over northern Mali and northwestern Mauritania (Figure 10b) as a result of three important meteorological features, namely: (1) lifting of dust by the strong near-surface turbulent wind behind the cold front, (2) the deepening daytime convective PBL, and (3) mixing of freshly emitted dust aerosols with the aged dust plume. At the same time, a smaller dust plume with significant dust loading appeared near the border of Senegal and Mauritania before the major dust front passed that region.

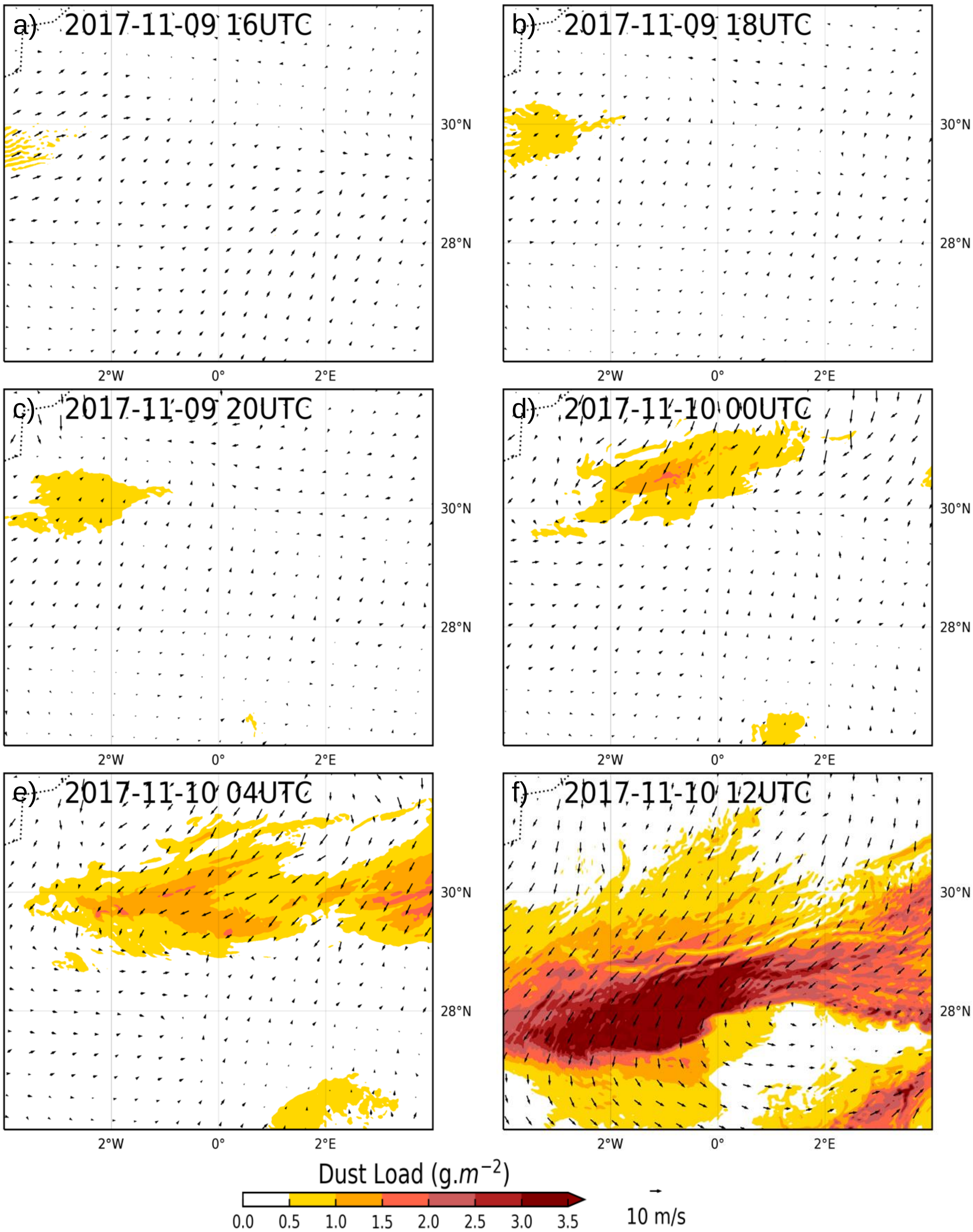

401 **Figure 9.** WRF-CHEM simulated (2-km) 10-meter wind vectors and dust load (shaded) at (a)
402 1600 UTC 9 November, (b) 1800 UTC 9 November, (c) 2000 UTC 9 November, (d) 0000 UTC
403 10 November, (e) 0400 UTC 10 November, and (f) 1200 UTC 10 November 2017.

By 1500 UTC on the 12th, the smaller dust plume, that first appeared near the border of Senegal and Mauritania, reached the Cape Verde Islands. At the same time, dust loading again increased near the coast of Mauritania (Figure 10c) due to the arrival of the strong dust storm from the Northeast paired with the growing daytime PBL and mixing of freshly emitted dust with the older dust plume. Finally, this large dust plume reached the Cape Verde Islands by 12 UTC on the 13th (Figure 10d).

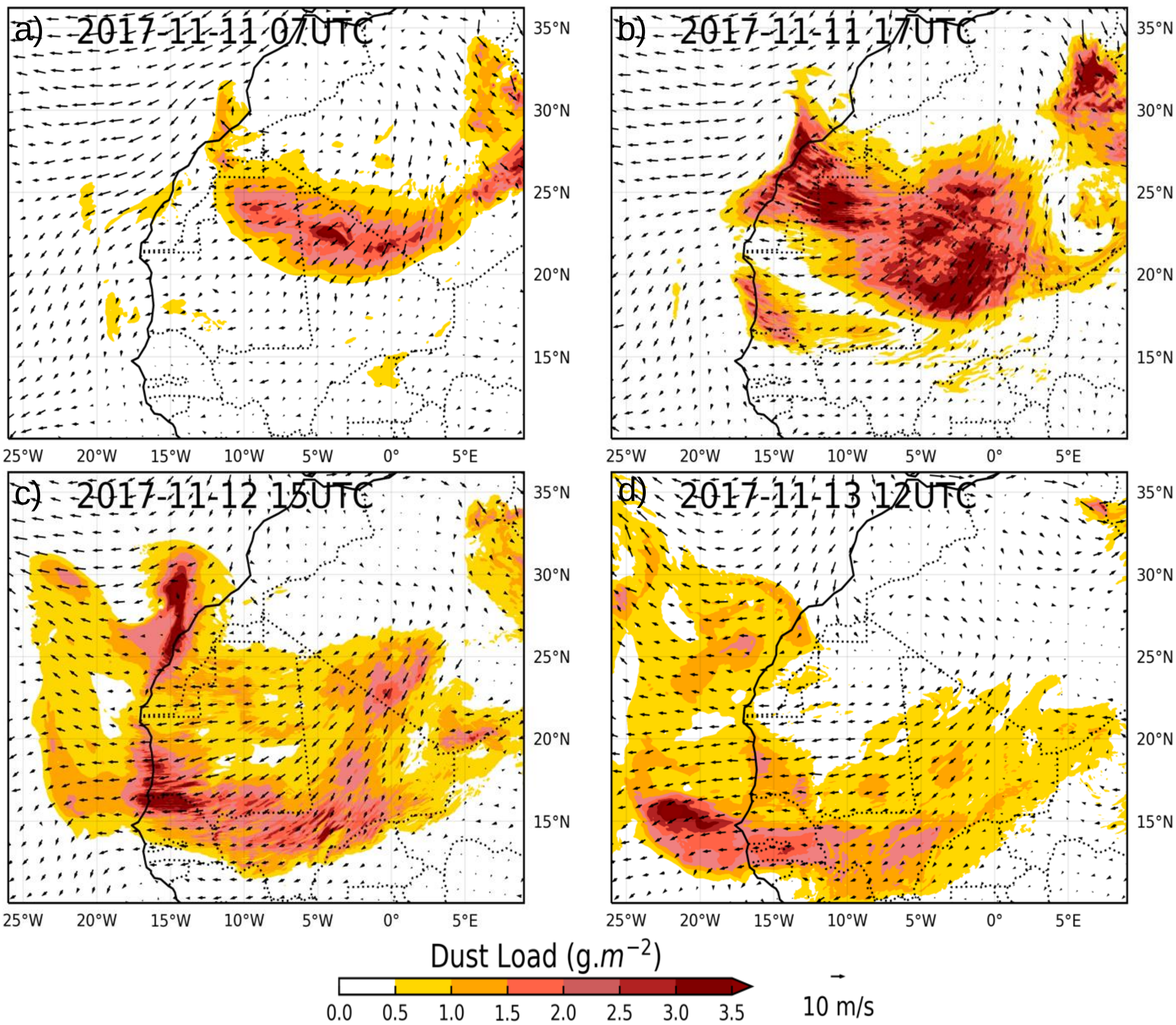

Figure 10. WRF-CHEM simulated (6-km) 10-meter wind vectors and dust load (shaded) valid for (a) 0700 UTC 11 November, (b) 1700 UTC 11 November, (c) 1500 UTC 12 November, and (d) 1200 UTC 13 November 2017.

In summary, the WRF-CHEM simulation indicated that the offshore dust plume over the Cape Verde Islands was the result of two distinct dust plumes consisting of composite emissions from several individual emission and lofting events. The smaller-scale dust plume that formed near the coast of Mauritania and Senegal was followed by the major dust plume consistent with the observations at Boa Vista Rabil station (161 in Figure 1a), in the Cape Verde Islands (Section 3.1.1).

4.2.2 Signals of a density current and internal bore

Investigating the small-scale structure of the dust event in more detail revealed the occurrence of a density current and internal bore. For their analysis, we used our 2km model simulation results and focused on the lee side of the Atlas Mountains. It needs to be reiterated here that the lack of a dense surface station network forces us to rely on numerical modeling to analyze these features. Figure 11 presents the time evolution of the vertical cross-sections of potential temperature, wind, and dust concentration along the 1°W transect.

At 2100 UTC on the 9th, cooler air relative to the ambient environment started to propagate downhill on the lee side of the Atlas Mountains causing the signal of a density current equatorward of the Mountains as indicated by the significant strong along-stream temperature gradient and sinking motion near 31.3°N (Figure 11a). Density currents are a type of flow in a fluid formed as a result of descending cool air and are one of the important mechanisms for dust emission over North Africa (e.g., Allen et al., 2013). One hour later, at 2200 UTC, strong sinking motion behind the cold front near 30.9°N added credibility to the assertion that this feature was a density current (Figure 11b). The putative density current continued to strengthen for several hours while propagating equatorward (Figures 11c and 11d).

At 0400 UTC on the 10th, the density current transitioned to a feature that had characteristics consistent with a bore equatorward of 29°N, when the density current impinged on the low-level stable layer (Figure 11e). Bore formation occurs when the density/gravity current encroaches on or perturbs the near-surface stable air (Koch et al., 2008). The along-stream horizontal scale of the putative bore continued to grow from 0400 UTC onwards for 2 hours while propagating downstream (Figures 11e and 11f). During this period, the dust load started to increase in the region of the bore structure. Beginning at 0600 UTC on the 10th, the density current and bore merged producing a density current-like cold front (Figures 11g and 11h) as in the case of a prefrontal bore formation on the lee of the Rocky Mountains during the 13-14 April 1986 lee cyclone, dust storms, and other severe weather events (Cram et al., 1991; Kaplan & Karyampudi, 1992a,b; Karyampudi et al., 1995a,b). The formation of an undular bore requires a low-level statically stable layer. The presence of the statically stable layer, in this case, is indicated by the compressed isentropes near the ground, which are capped by the less stable residual mixed layer (Figures 11g and 11h). Karyampudi et al. (1995b) also reiterate the importance of near-surface inflow to aid the stable layer in the ducting process. Thus, as in our case, the density current was initiated by the interaction of the flow with the complex terrain of the Atlas Mountains.

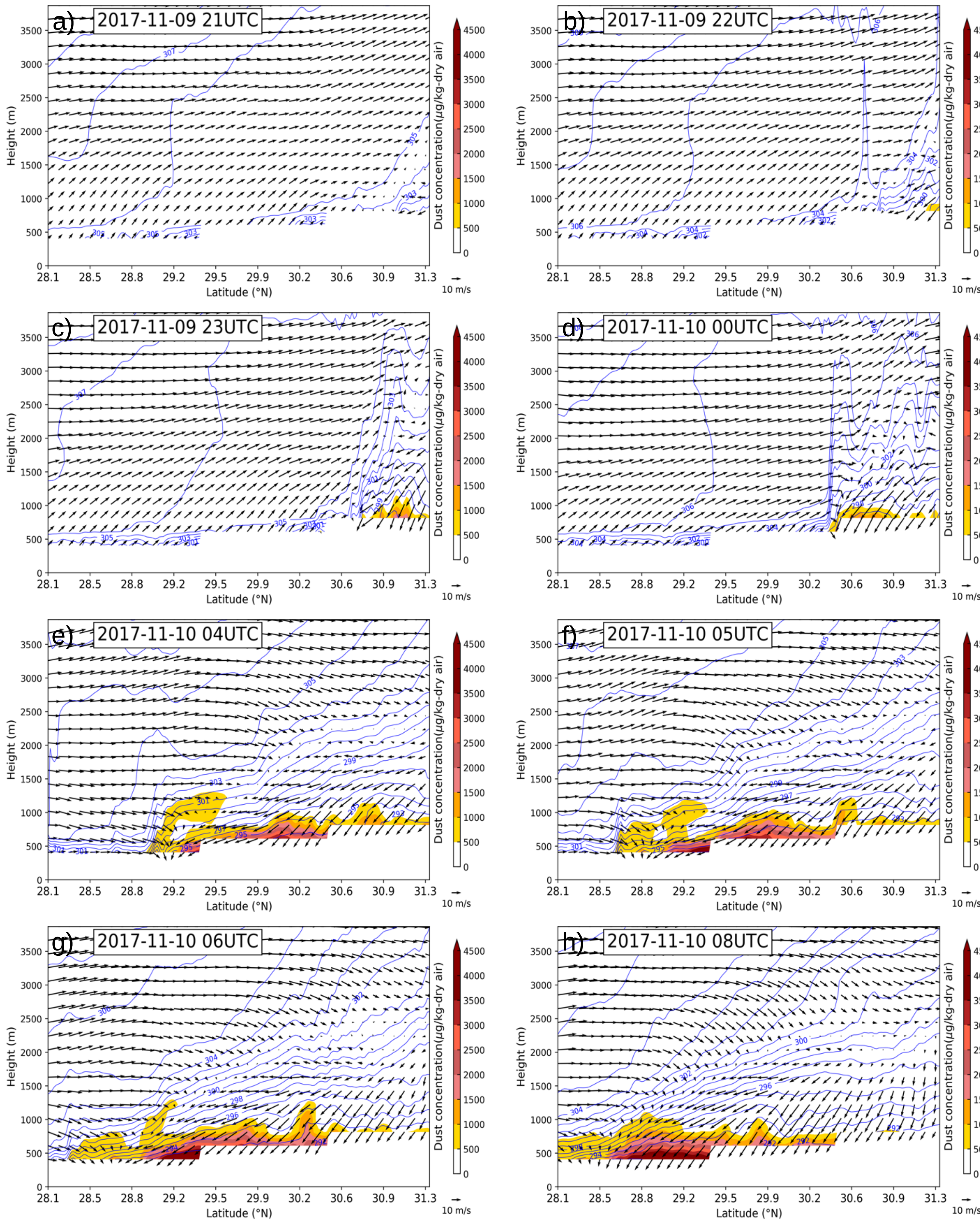

454 **Figure 11.** WRF-CHEM simulated (2-km) vertical cross-sections of dust concentration (shaded), wind vectors, and potential temperature (blue contours) along 1°W transect at (a) 2100 UTC 9 November, (b) 2200 UTC 9 November, (c) 2300 UTC 9 November, (d) 0000 UTC 10

November, (e) 0400 UTC 10 November, (f) 0500 UTC 10 November, (g) 0600 UTC 10 November, and (h) 0800 UTC 10 November 2017.

4.2.3 Dust triggering mechanisms and spatio-temporal evolution of dust frontogenesis

We investigate the role of the bore and density current in dust emission and dust frontogenesis next. Again, we use the charts of the 2km simulation results. Now we focus on the evolution of the convergence zone, dust aerosol concentrations, and PBL turbulence kinetic energy (PBL TKE).

At 1700 UTC on the 9th, the West African heat low, located on the lee side of the Saharan Atlas Mountains near 2.5°W, 31°N (Figure 12a), dominated the regional weather. We define the heat low as the area of high surface temperature and low surface pressure consistent with Lavaysse et al. (2009). One hour later, the nearby SYNOP station Beni-Abbes (100 in Figure 1a) in Bechar Province, Algeria, recorded a MSLP value of 1011.9 hPa. For two hours, from 1800 UTC to 2000 UTC, the heat low was stationary (Figures 12b). During this period, a narrow band of dust appeared over the western part of the Beni Abbes location (Figures 12b and 12c). This narrow band of dust, prior to the major dust front, was associated with the southwesterly low-level wind into the developing leeside surface (heat) low over Oued Dra River Valley near the Morocco/Algeria border. The southwesterly low-level wind deflated dust from the surface and transferred it northeastward before the formation of the nocturnal PBL and dust frontogenesis. At 2200 UTC, the density current ahead of the cold front interacted with the leeside surface low (Figures 11b and 12c) near 31°N. Also, a shallow PBL TKE [TKE up to ~300 meter above ground level (AGL)] signal formed near the heat low region which is indicated by the higher values of PBL TKE near 31.3°N (Figure 13a). These features indicate that the density current forced the near-surface flow to create a confluence region during the 2000-2200 UTC time period on the 9th which was enhanced by the formation of shallow near-surface TKE. The surface heat low further intensified and shifted slightly farther east to the Beni Abbes by 2300 UTC (Figure 12d).

At 0000 UTC on the 10th, the northerly and west-southwesterly flows amplified and were followed by weak near-surface TKE which appeared near the confluence region located ahead of the major cold front around 1°W, 30°N (Figures 9d and 13b). A significant amount of the dust loading occurred to the northeast of the intensifying confluence region (Figure 9d). These features indicate the signal of an intensifying confluence zone and the incipient stage of the dust frontogenesis. The surface low continued moving southeast under the influence of the cold front, where the dust front further intensified.

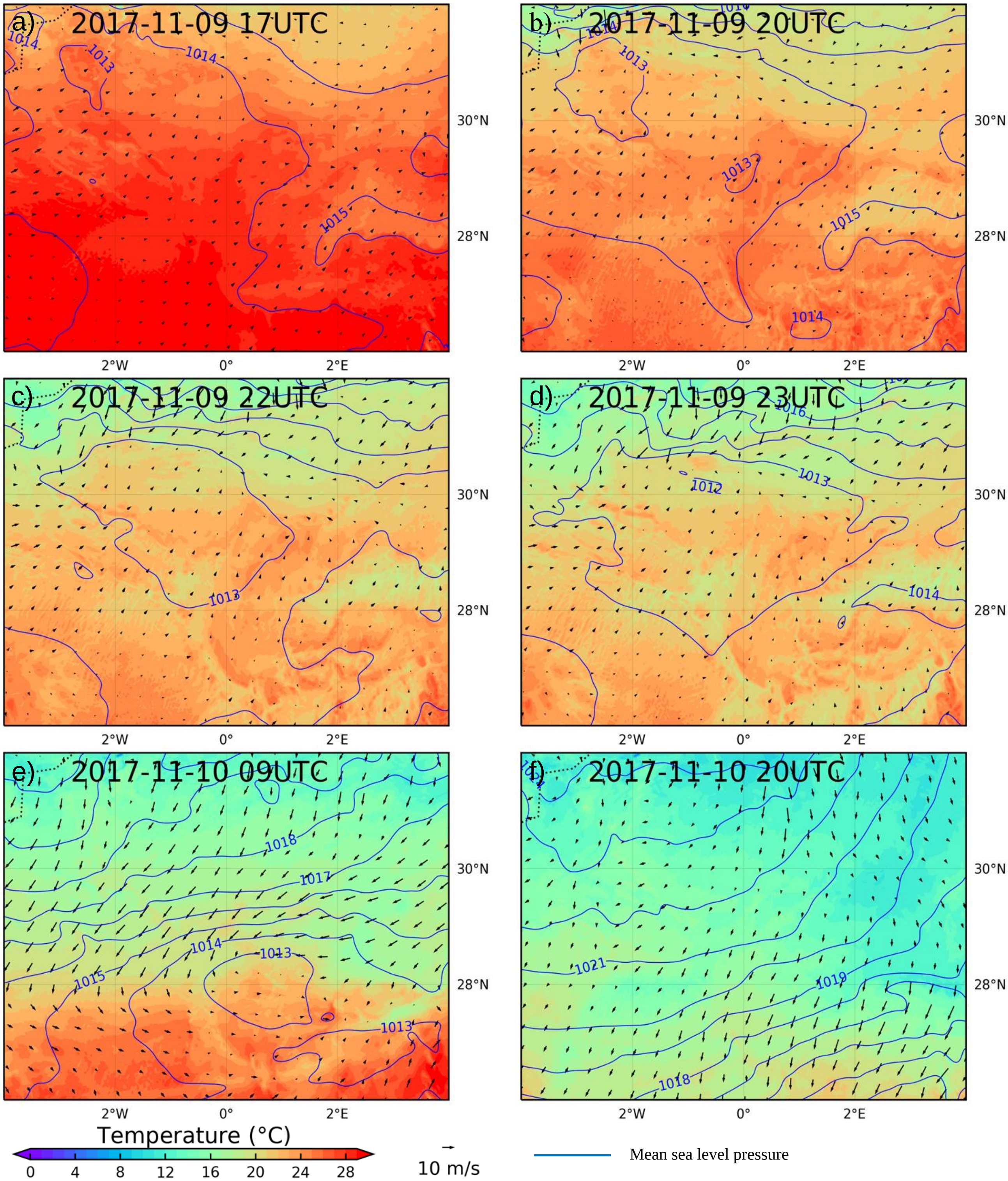

Figure 12. WRF-CHEM simulated (2-km) 10-meter wind vectors, 2-meter temperature (shaded), and MSLP in hPa (blue contours) valid for (a) 1700 UTC 9 November, (b) 2000 UTC 9

November, (c) 2200 UTC 9 November, (d) 2300 UTC 9 November, (e) 0900 UTC 10 November, and (f) 2000 UTC 10 November 2017.

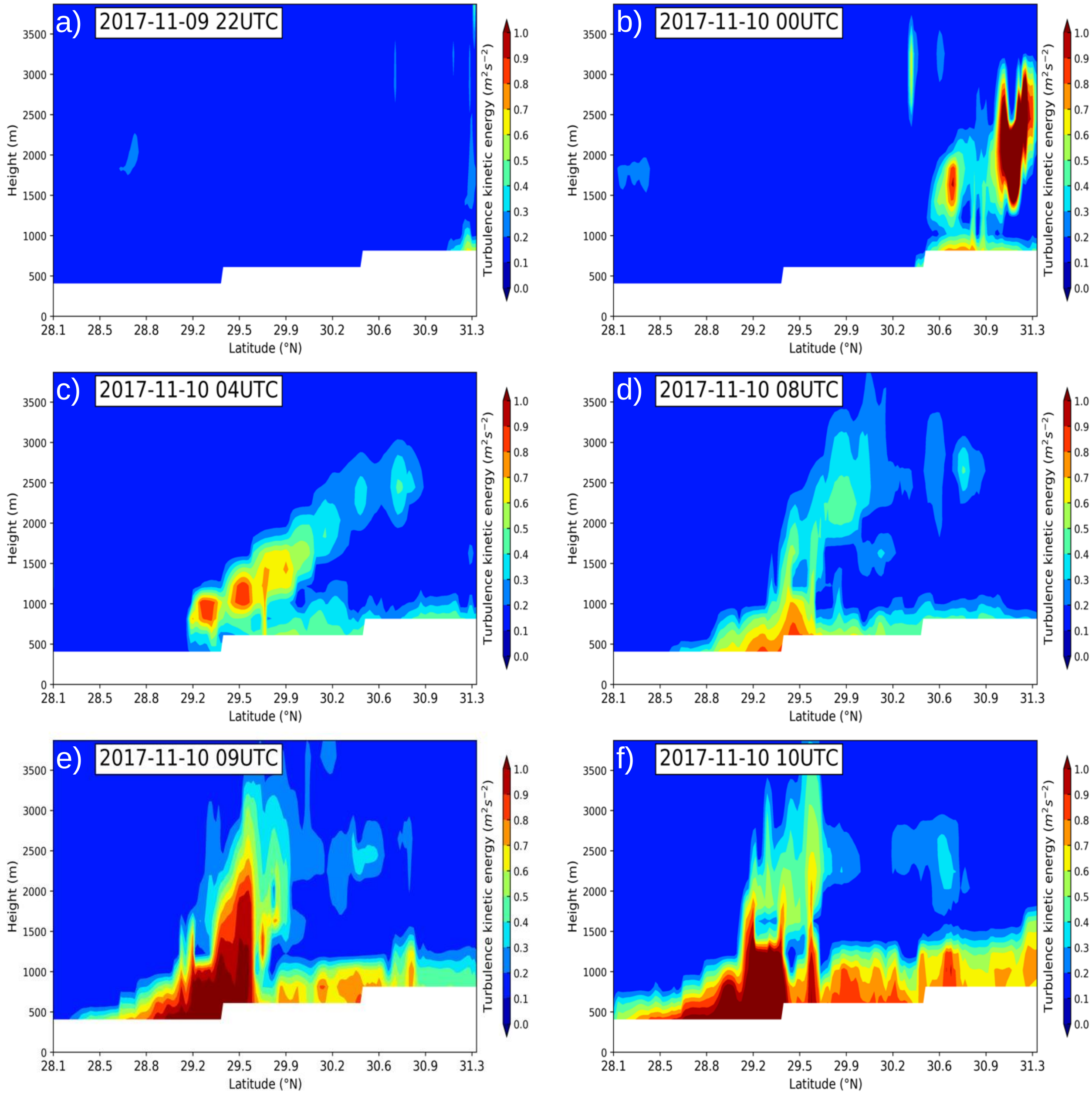

Figure 13. WRF-CHEM simulated (2-km) PBL TKE valid for (a) 2200 UTC 9 November, (b) 0000 UTC 10 November, (c) 0400 UTC 10 November, (d) 0800 UTC 10 November, (e) 0900 UTC 10 November, and (f) 1000 UTC 10 November 2017.

At 0400 UTC, the bore developed equatorward of 30°N along the 1°W transect as PBL TKE increased near the confluence region and subsequently accumulated more dust along the 1°W transect (Figures 9e and 11e). For a few more hours, while it was propagating equatorward, the dust front strengthened continuously. Noticeable features occurred at around 0800 UTC after sunrise during which both the cool density current and the increased PBL TKE behind the large-scale cold front resulted in upward mixing of dust aerosols and thus an intensification of the dust front in the sense of larger aerosol concentrations (Figures 11h and 13d). The intensification of the dust front is indicated by the increased (primarily along-stream) sharp gradient of dust loading near 28.7°N.

A new mesolow (heat low) with a magnitude of 1013 hPa formed near Adrar in Algeria at 0900 UTC associated with daytime heating (see pressure contours around 0-1.5°E, 27-29°N, Figure 12e). Consistent with the simulation, the SYNOP station Adrar recorded an MSLP observation of 1013.8 hPa and near-surface temperature of 20.8°C. At the same time, the north-northwesterly winds and PBL TKE increased behind the cold front (Figures 12e and 13e). This newly formed heat low with a cyclonic flow and the north-northwesterly rotating winds increased the magnitude of the convergence at the eastern side of the low. Paired with the increasing PBL TKE, the dust frontogenesis intensified and became visible as a boundary between the dust-laden air behind the cold front and the heat low. Dust frontogenesis continued to strengthen and its spatial extent expanded during the day. At 2000 UTC on the 10^{th}, the heat low propagated towards the poleward side of the Hoggar Mountains and the dust front orientation became southwest to northeast with significant dust loading behind the leading edge (Figure 12f).

After 2000 UTC, the heat low and PBL TKE both weakened following by a stabilization of the near-surface air. The Coriolis force, acting on the winds, turned the flow anticyclonically, seen as a wind shift from northerlies to easterlies. Additionally, the Hoggar Mountains blocked a significant amount of dust-laden air at low levels limiting the equatorward advection. Taken together, the easterly and northeasterly winds transported the dust aerosols further westwards.

In summary, the evolution of dust frontogenesis occurred as follows: (1) at around 1600 UTC on the 9^{th} southwesterly low-level flow propagated into a developing leeside heat low over the Oued Dra River Valley near the Morocco/Algeria border, (2) the flow intensified and transferred near-surface dust aerosols east-northeastwards, and (3) was followed by the formation of the nocturnal PBL and dust frontogenesis. For two hours, from 2000-2200 UTC, a density current forced the north-northeasterly surface flow down the Saharan Atlas Mountains ahead of the larger-scale cold front and started to create the convergence of dust-laden air near the leading edge of the dust front. This convergent flow was aided by a shallow PBL TKE buildup below the stable lid of the nocturnal PBL. Incipient strong dust frontogenesis occurred around 0000 UTC on the 10^{th} as the convergence strengthened ahead of the weak surface TKE and strengthening boundary between the northerly and west-southwesterly flow. After sunrise, at 0800 UTC, PBL TKE increased due to the daytime deepening PBL, and the dust front quickly sharpened as cold air and PBL TKE behind the leading edge of the larger-scale cold front increased dust-emitting winds at the surface and lofting of dust into the PBL. The daytime heating led to the formation of a new heat low, centered around 0-1°E, 28°N by 0900 UTC, causing convergence of the associated winds with the north-northwesterly flow of the cold front. On the following night the flow turned anticyclonically towards the west as a result of the Coriolis force which reoriented the dust front for propagation towards the Atlantic Ocean.

4.3 Backward Trajectories

We use backward trajectories as an additional test for the identification of transport pathways of the dust-laden air arriving in Mindelo on Sao Vicente, Cape Verde. Five days of

HYSPLIT back trajectories were calculated starting at 1200 UTC 13 November, the time when the dust concentration was largest. The analysis showed converging air parcels originating near southern France and northern Mali (Figure 14). The sinking of air parcels was initiated before reaching the southern flank of the Saharan Atlas Mountains consistent with: (1) the strong deep tropospheric thermally indirect circulation and (2) the lowering of potential temperature due to low-level cold air advection during the initial phase of dust ablation at 0600 UTC 10 November. Most of the air parcels that reached Mindelo came first from the southern flank of the Saharan Atlas Mountains and second from the plains of northern Mali crossing the coast of Mauritania and Senegal. The air parcels from northern Mali were clearly from low-levels and a slight ascent occurred during their transport before arriving at low-levels at Mindelo. The lifting of air-parcels during the dust front's course of motion was in large part due to the turbulent mixing within the growing daytime and convective PBL consistent with a large magnitude of PBL TKE. These features indicate that air parcels that arrived at Mindelo during the afternoon of 13 November at low-levels descended from upper-levels over North Africa as a result of a strong thermally indirect circulation and formed in part as the result of the strong dust-transporting Harmattan surge.

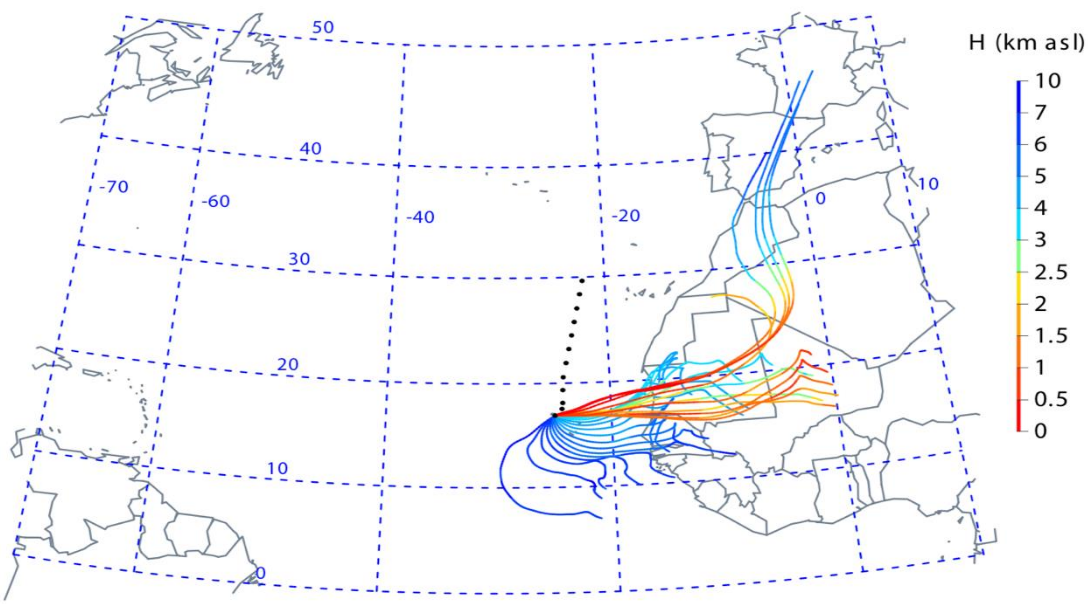

Figure 14: 120-hour back trajectories (ERA-Interim data) arriving at Mindelo, Cape Verde Islands at different heights and starting at 1800 UTC 13 November. Filled black circles are the MSM68/2 North Atlantic expedition ship positions every 6 hours from 11 November 0000 UTC till 13 November 1800 UTC 2017 (Fiedler, 2018).

5 Summary and conclusions

This study analyzed the multi-scale atmospheric processes responsible for the early Harmattan season dust outbreak over the Cape Verde Islands on 13 November 2017 that lead to a major disruption in local air traffic utilizing the reanalysis datasets and the WRF-CHEM simulation. To the authors' knowledge, this is the first detailed study of the evolution of the dust frontogenesis in the case of a Harmattan surge utilizing high-resolution WRF-CHEM model simulations with horizontal resolution as fine as 2km. The highlights in the evolution of the dust outbreak include: (1) the intrusion of cool air into North Africa following the previous occurrence of two Rossby wave breaking events, (2) the formation and propagation of an undular bore on the lee side of the Saharan Atlas Mountains involving a density current from the Atlas Mountains with the subsequent southward advection of dust aerosols, and (3) the interaction between the southwestward propagating dust front and growing daytime convective PBL leading to the several 100km long distance transport over land towards the ocean. Dust arrived at Mindelo on the afternoon of 13 November. The dust aerosols over the Cape Verde Islands are the result of two distinct dust plumes. The smaller-scale dust plume that formed near the coast of Mauritania and Senegal, ahead of the primary dust front, was followed by a major dust plume.

The summary of the mechanism leading to the dust aerosol transport to the Cape Verde Islands is depicted graphically in Figure 15. At the synoptic scale, two RWB and linking non-linear wave reflection significantly contributed to wave amplification over the Eastern North Atlantic Ocean and resulted in the intrusion of air with high PV into the North African continent. The pressure surge associated with the cold air intrusion into North Africa over the Saharan Atlas Mountains resulted in strong near-surface winds that mobilized dust, as is known for classical Harmattan surges (e.g., Fiedler et al. 2015, Pokharel et al., 2017). At the mesoscale, the density current associated with the cold air inflow over the Atlas Mountains resulted in triggering multiple bores downstream. Each bore perturbed the vertical distribution of dust aerosols and, together with the subsequent increase in PBL TKE from the daytime heating, contributed to the dust frontogenesis. Dust became confined behind the leading edge of the cold surge and interacted with the growing convective daytime Saharan PBL that further increased the dust aerosol loading. The increasing dust aerosol burden at the different stages of the continental-scale storm was primarily due to the development of a daytime convective PBL associated with the strong surface heating while simultaneously propagating south-westward and later westward.

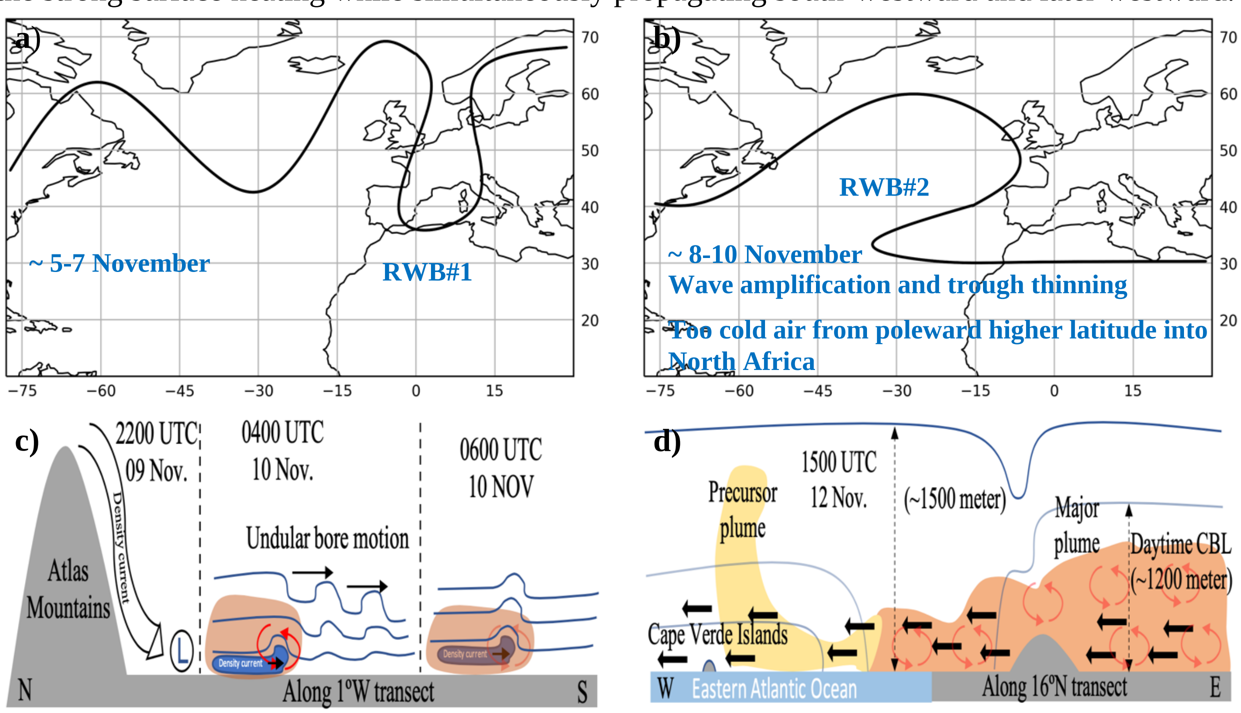

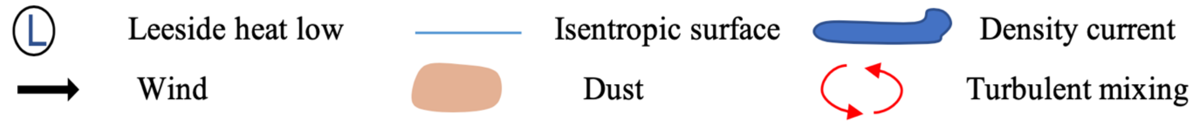

Figure 15. The schematic depiction of the time and region of double Rossby wave breaks in the polar stream (a and b), density current, undular bore formation, and transition of bore to the density current-like cold front (c). The subsequent sequence of dual dust plumes towards the Cape Verde Islands (d) is also shown.

Acknowledgments

The authors would like to thank the German Science Foundation for enabling the North Atlantic Expedition MSM 68/2 with research vessel RV Maria S. Merian for collecting AOD measurements quality controlled by the Maritime Aerosol Network (MAN) as part of NASA's Aerosol Robotic Network (AeroNet). We also want to thank the National Center for Atmospheric Research (NCAR) Computational and Information System Laboratory and the National Science Foundation (NSF) for providing the high-performance computing support from the Cheyenne (doi:10.5065/D6RX99HX). We also acknowledge the various institutions for providing the following datasets and model: (1) National Climatic Data Center for METAR and SYNOP datasets (ftp://ftp.ncdc.noaa.gov/pub/data/noaa), (2) ECMWF for the ERA-Interim reanalysis data (https://www.ecmwf.int/en/forecasts/datasets/reanalysis-datasets/era-interim), (3) EUMETSAT for the SEVIRI MSG data (available at https://eoportal.eumetsat.int/ after registration), (4) NOAA/ESRL for the HYSPLIT model, and (5) the University of Wyoming for radiosonde sounding data. This research was not funded under any project-specific grant.

References

Abatzoglou, J. T., & Magnusdottir, G. (2004). Nonlinear planetary wave reflection in the troposphere. *Geophysical Research Letters*, *31*(9), 1–4. https://doi.org/10.1029/2004GL019495

Allen, C. J. T., Washington, R., & Engelstaedter, S. (2013). Dust emission and transport mechanisms in the central Sahara: Fennec ground-based observations from Bordj Badji Mokhtar, June 2011. *Journal of Geophysical Research Atmospheres*, *118*(12), 6212–6232. https://doi.org/10.1002/jgrd.50534

Burton, R. R., Devine, G. M., Parker, D. J., Chazette, P., Dixon, N., Flamant, C., & Haywood, J. M. (2013). The harmattan over West Africa: Nocturnal structure and frontogenesis. *Quarterly Journal of the Royal Meteorological Society*, *139*(674), 1364–1373. https://doi.org/10.1002/qj.2036

Chen, F., & Dudhia, J. (2001). Coupling and advanced land surface-hydrology model with the Penn State-NCAR MM5 modeling system. Part I: Model implementation and sensitivity. Monthly Weather Review, 129(4), 569–585. https://doi.org/10.1175/1520-0493(2001)129<0569:CAALSH>2.0.CO;2

Cram, J. M., Kaplan, M. L., Mattocks, C. A., & Zack, J. W. (1991). The use and analysis of profiler winds to derive mesoscale height and temperature fields: simulation and real-data experiments. *Monthly Weather Review*, *119*(4), 1040–1056. https://doi.org/10.1175/1520-

0493(1991)119<1040:TUAAOP>2.0.CO;2

Dee, D. P., Uppala, S. M., Simmons, A. J., Berrisford, P., Poli, P., Kobayashi, S., et al. (2011). The ERA-Interim reanalysis: Configuration and performance of the data assimilation system. *Quarterly Journal of the Royal Meteorological Society*, *137*(656), 553–597. https://doi.org/10.1002/qj.828

Dudhia, J. (1989). Numerical study of convection observed during the Winter Monsoon Experiment using a mesoscale two-dimensional model. *Journal of the Atmospheric Sciences*, 46(20), 3077-3107. https://doi.org/10.1175/1520-0469(1989)046<3077:NSOCOD>2.0.CO;2

Ek, M. B., Mitchell, K. E., Lin, Y., Rogers, E., Grunmann, P., Koren, V., et al. (2003). Implementation of Noah land surface model advances in the National Centers for Environmental Prediction operational mesoscale Eta model. *Journal of Geophysical Research D: Atmospheres*, 108(D22), 8851. https://doi.org/10.1029/2002JD003296

Fiedler, S., 2018. Expedition to the North Atlantic with RV MARIA S. MERIAN. *Berichte zur Erdsystemforschung*, 211, doi: 10.17617/2.3006588

Fiedler, S., Kaplan, M. L., & Knippertz, P. (2015). The importance of Harmattan surges for the emission of North African dust aerosol. *Geophysical Research Letters*, *42*(21), 9495–9504. https://doi.org/10.1002/2015GL065925

Gama, C., Tchepel, O., Baldasano, J. M., Basart, S., Ferreira, J., Pio, C., et al. (2015). Seasonal patterns of Saharan dust over Cape Verde - a combined approach using observations and modelling. *Tellus, Series B: Chemical and Physical Meteorology*, *67*(1), 24410. https://doi.org/10.3402/tellusb.v67.24410

Ginoux, P., Chin, M., Tegen, I., Prospero, J. M., Holben, B., Dubovik, O., & Lin, S.-J. (2001). Sources and distributions of dust aerosols simulated with the GOCART model. *Journal of Geophysical Research: Atmospheres*, *106*(D17), 20255–20273. https://doi.org/10.1029/2000JD000053

Grell, G. A., Peckham, S. E., Schmitz, R., Mckeen, S. A., Frost, G., Skamarock, W. C., & Eder, B. (2005). Fully coupled '" online "' chemistry within the WRF model, *39*, 6957–6975. https://doi.org/10.1016/j.atmosenv.2005.04.027

Heinold, B., Knippertz, P., Marsham, J. H., Fiedler, S., Dixon, N. S., Schepanski, K., et al. (2013). The role of deep convection and nocturnal low-level jets for dust emission in summertime West Africa: Estimates from convection-permitting simulations. *Journal of Geophysical Research: Atmospheres*, *118*(10), 4385–4400. https://doi.org/10.1002/jgrd.50402

Janjic, Z. (2002). Nonsingular Implementation of the Mellor-Yamada Level 2.5 Scheme in the NCEP Meso model. NCEP Office Note 437, pp 61.

Janjic, Z. I. (1994). The step-mountain eta coordinate model: further developments of the convection, viscous sublayer, and turbulence closure schemes. *Monthly Weather Review*, *122*(5), 927–945. https://doi.org/10.1175/1520-0493(1994)122<0927:TSMECM>2.0.CO;2

Kaplan, M. L., & Karyampudi, V. M. (1992a). Meso-Beta Scale Numerical Simulations of Terrain Drag-Induced Along-Stream Circulations. Part I: Midtropospheric Frontogenesis.

Meteorol. Atmos. Phys (Vol. 49), 133-156.

Kaplan, M. L., & Karyampudi, V. M. (1992b). Meso-Beta Scale Numerical Simulations of Terrain Drag-Induced Along-Stream Circulations. Part II: Concentration of Potential Vorticity Within Dryline Bulges. *Meteorol. Atmos. Phys* (Vol. 49), 157-185.

Karyampudi, V. M., Kaplan, M. L., Koch, S. E., & Zamora, R. J. (1995). The Influence of the Rocky Mountain on the 13–14 April 1986 Severe Weather Outbreak. Part I: Mesoscale Lee Cyclogenesis and Its Relationship to Severe Weather and Dust Storms. *Monthly Weather Review*, *123*(5), 1394–1422. https://doi.org/10.1175/1520-0493(1995)123<1394:tiotrm>2.0.co;2

Karyampudi, V. M., Koch, S. E., Chen, C., Rottman, J. W., & Kaplan, M. L. (1995). The Influence of the Rocky Mountains on the 13–14 April 1986 Severe Weather Outbreak. Part II: Evolution of a Prefrontal Bore and Its Role in Triggering a Squall Line. *Monthly Weather Review*, *123*(5), 1423–1446. https://doi.org/10.1175/1520-0493(1995)123<1423:tiotrm>2.0.co;2

Klose, M., Shao, Y., Karremann, M. K., & Fink, A. H. (2010). Sahel dust zone and synoptic background. *Geophysical Research Letters*, *37*(9), 1–6. https://doi.org/10.1029/2010GL042816

Knippertz, P., & Fink, A. H. (2006). Synoptic and dynamic aspects of an extreme springtime Saharan dust outbreak. *Quarterly Journal of the Royal Meteorological Society*, *132*(617), 1153–1177. https://doi.org/10.1256/qj.05.109

Koch, S. E., Flamat, C., Wilson, J. W., Gentry, B. M., & Jamison, B. D. (2008). An atmospheric soliton observed with Doppler radar, differential absorption lidar, and a molecular Doppler lidar. *Journal of Atmospheric and Oceanic Technology*, *25*(8), 1267–1287. https://doi.org/10.1175/2007JTECHA951.1

Lavaysse, C., Flamant, C., Janicot, S., Parker, D. J., Lafore, J. P., Sultan, B., & Pelon, J. (2009). Seasonal evolution of the West African heat low: A climatological perspective. *Climate Dynamics*, *33*(2–3), 313–330. https://doi.org/10.1007/s00382-009-0553-4

Mellor, G. L., & Yamada, T. (1974). A Hierarchy of Turbulence Closure Models for Planetary Boundary Layers. *Journal of the Atmospheric Sciences*, *31*(7), 1791–1806. https://doi.org/10.1175/1520-0469(1974)031<1791:ahotcm>2.0.co;2

Messori, G., & Caballero, R. (2015). On double Rossby wave breaking in the North Atlantic. *Journal of Geophysical Research: Atmospheres*, *120*(21), 11,129-11,150. https://doi.org/10.1002/2015JD023854

Mlawer, E. J., Taubman, S. J., Brown, P. D., Iacono, M. J., & Clough, S. A. (1997). Radiative transfer for inhomogeneous atmospheres: RRTM, a validated correlated-k model for the longwave. *Journal of Geophysical Research D: Atmospheres*, *102*(14), 16663–16682. https://doi.org/10.1029/97jd00237

Moulin, C., Lambert, C. E., Dayan, U., Masson, V., Ramonet, M., Bousquet, P., et al. (1998). Satellite climatology of African dust transport in the Mediterranean atmosphere. *Journal of Geophysical Research Atmospheres*, *103*(D11), 13137–13144. https://doi.org/10.1029/98JD00171

Pey, J., Querol, X., Alastuey, A., Forastiere, F., & Stafoggia, M. (2013). African dust outbreaks over the Mediterranean Basin during 2001-2011: PM10concentrations, phenomenology and trends, and its relation with synoptic and mesoscale meteorology. *Atmospheric Chemistry and Physics*, *13*(3), 1395–1410. https://doi.org/10.5194/acp-13-1395-2013

Pokharel, A. K., Kaplan, M. L., & Fiedler, S. (2017). The Role of Jet Adjustment Processes in Subtropical Dust Storms. *Journal of Geophysical Research: Atmospheres*, *122*(22), 12,122-12,139. https://doi.org/10.1002/2017JD026672

Prospero, J. M. (1999). Long-range transport of mineral dust in the global atmosphere: Impact of African dust on the environment of the southeastern United States. *Proceedings of the National Academy of Sciences*, *96*(7), 3396–3403. https://doi.org/10.1073/pnas.96.7.3396

Prospero, Joseph M., & Mayol-Bracero, O. L. (2013). Understanding the transport and impact of African dust on the Caribbean Basin. *Bulletin of the American Meteorological Society*, *94*(9), 1329–1337. https://doi.org/10.1175/BAMS-D-12-00142.1

Prospero, Joseph M., Ginoux, P., Torres, O., Nicholson, S. E., & Gill, T. E. (2002). Environmental characterization of global sources of atmospheric soil dust identified with the Nimbus 7 Total Ozone Mapping Spectrometer (TOMS) absorbing aerosol product. *Reviews of Geophysics*, *40*(1), 1–31. https://doi.org/10.1029/2000RG000095

Reinfried, F., Tegen, I., Heinold, B., Hellmuth, O., Schepanski, K., Cubasch, U., et al. (2009). Simulations of convectively-driven density currents in the Atlas region using a regional model: Impacts on dust emission and sensitivity to horizontal resolution and convection schemes. *Journal of Geophysical Research Atmospheres*, *114*(8), 1–13. https://doi.org/10.1029/2008JD010844

Roberts, A. J., & Knippertz, P. (2014). The formation of a large summertime Saharan dust plume: Convective and synoptic-scale analysis. *Journal of Geophysical Research*, *119*(4), 1766–1785. https://doi.org/10.1002/2013JD020667

Solomos, S., Kalivitis, N., Mihalopoulos, N., Amiridis, V., Kouvarakis, G., Gkikas, A., et al. (2018). From tropospheric folding to Khamsin and Foehn winds: How atmospheric dynamics advanced a record-breaking dust episode in Crete. *Atmosphere*, *9*(7), 240. https://doi.org/10.3390/atmos9070240

Stein, A. F., Draxler, R. R., Rolph, G. D., Stunder, B. J. B., Cohen, M. D., & Ngan, F. (2015). NOAA's HYSPLIT atmospheric transport and dispersion modeling system. *Bulletin of the American Meteorological Society*, *96*(12), 2059–2077. https://doi.org/10.1175/BAMS-D-14-00110.1

Thompson, G., Field, P. R., Rasmussen, R. M., & Hall, W. D. (2008). Explicit forecasts of winter precipitation using an improved bulk microphysics scheme. Part II: Implementation of a new snow parameterization. *Monthly Weather Review*, *136*(12), 5095–5115. https://doi.org/10.1175/2008MWR2387.1

Van der Does, M., Knippertz, P., Zschenderlein, P., Giles Harrison, R., & Stuut, J. B. W. (2018). The mysterious long-range transport of giant mineral dust particles. *Science Advances*, *4*(12), eaau2768. https://doi.org/10.1126/sciadv.aau2768

Varga, G., Kovács, J., & Újvári, G. (2013). Analysis of Saharan dust intrusions into the

Carpathian Basin (Central Europe) over the period of 1979-2011. *Global and Planetary Change*, *100*, 333–342. https://doi.org/10.1016/j.gloplacha.2012.11.007

Washington, R., Todd, M., Middleton, N. J., & Goudie, A. S. (2003). Dust-storm source areas determined by the total ozone monitoring spectrometer and surface observations. *Annals of the Association of American Geographers*, *93*(2), 297–313. https://doi.org/10.1111/1467-8306.9302003

Wiegand, L., & Knippertz, P. (2014). Equatorward breaking Rossby waves over the North Atlantic and Mediterranean region in the ECMWF operational Ensemble Prediction System. *Quarterly Journal of the Royal Meteorological Society*, *140*(678), 58–71. https://doi.org/10.1002/qj.2112